Space Science Reviews (2023) 219:61
https://doi.org/10.1007/s11214-023-01003-8

Investigating Europa's Radiation Environment with the Europa Clipper Radiation Monitor

Richard Meitzler[1] · Insoo Jun[2] · Ryan Blase[3] · Timothy Cassidy[4] · Roger Clark[5] · Corey Cochrane[2] · Sam Fix[1] · Randy Gladstone[3] · John Goldsten[1] · Murthy Gudipati[2] · Kevin Hand[2] · Bryana Henderson[2] · Xianzhe Jia[6] · Joshua Kammer[3] · Peter Kollmann[1] · Alfred McEwen[7] · Heather Meyer[1] · Tom Nordheim[2] · Chris Paranicas[1] · Carol Paty[8] · Kurt Retherford[3] · Elias Roussos[9] · Abigail Rymer[1] · Todd Smith[1] · Joe Westlake[1] · Zach Yokley[1]

Received: 18 April 2023 / Accepted: 13 September 2023 / Published online: 13 October 2023

Abstract

We present an overview of the radiation environment monitoring program planned for the Europa Clipper mission. The harsh radiation environment of Jupiter will be measured by a dedicated Radiation Monitor (RadMon) subsystem, yielding mission accumulative Total Ionizing Dose (TID) and instantaneous electron flux measurements with a 1-Hz cadence. The radiation monitoring subsystem is comprised of a stand alone sensor assembly along with distributed TID assemblies at various locations on the spacecraft. The sensor assembly itself is made of a TID sensor stack using the Metal-Oxide Semiconducting Field-Effect Transistor (MOSFET) and a Charge Rate Monitor (CRM) that uses a stack of bulk charge collection plates. The TID measurements will provide the critical information about the overall radiation levels relevant to the degradation of electronics over time, and the electron flux data can serve as a proxy for the Internal ElectroStatic Discharge (IESD) environment by measuring the $>\sim 1$ MeV electron environment. In addition, the radiation monitoring subsystem data will be augmented by serendipitous radiation data from science instruments onboard. This will be enabled by careful modeling and analysis of opportunistic background data from potentially the following instruments: Europa Imaging System (EIS), Europa-Ultraviolet Spectrograph (Europa-UVS), Mapping Imaging Spectrometer for Europa (MISE), MAss Spectrometer for Planetary EXploration (MASPEX), Plasma Instrument for Magnetic Sounding (PIMS), and SUrface Dust Analyzer (SUDA). Based on the current analysis, these instruments will be most sensitive to >1 MeV electrons. As such, the high-energy electron data obtained by the radiation monitoring subsystem will be qualitatively and quantitatively enhanced by the high-energy electron data acquired by the instruments. The holistic radiation monitoring program for the mission will be an extensive collaboration among many teams across the flight and payload systems.

Although the radiation monitoring subsystem itself is an engineering resource for the mission, the collective data from the mission can also be used to improve the scientific understanding of the Jovian magnetosphere and the high-energy electron environment near

Europa Clipper: A Mission to Explore Ocean World Habitability
Edited by Haje Korth, Bonnie J. Buratti and David Senske

Extended author information available on the last page of the article

Europa, where the motion of charged particles is perturbed by the local electromagnetic environment. The data could also help in the understanding of the radiation modification of Europa surface compounds, which could subsequently help guide lab experiments to aid in understanding the origin and evolution of surface materials and in constraining the interpretation of observational data. To this end, the radiation monitoring subsystem is a useful resource for helping address the Europa Clipper mission's primary goal of assessing the habitability of Europa.

Keywords Europa Clipper mission · Radiation Monitor · RadMon · RadFET · Charge Rate Monitor

1 Introduction

The main objective of this paper is to describe the Jovian radiation environment monitoring program to be carried out by the Europa Clipper mission. This monitoring will be mainly achieved by the Radiation Monitor, hereinafter referred to as "RadMon", which is an engineering subsystem of the spacecraft, augmented by both planned and serendipitous radiation measurements by other science instruments onboard. The radiation-monitoring effort for the Europa Clipper mission will enhance our knowledge of the radiation environment in a number of ways. Improved characterization of Jupiter's radiation belts will be achieved, especially in the equatorial region between ∼8 and ∼50 Rj (representing the radial distance in Jovian radii, with Jupiter's radius Rj = 71,492 km), using measurement data from the dedicated radiation monitor unit, shielded assets, and information from the instruments. These measurements will provide invaluable real-time information about the charged particle environment that may affect the health of the spacecraft and will be used in diagnosing potential spacecraft anomalies (Fieseler et al. 2002). In addition, these data can inform spacecraft operations in real-time to maximize the science return. Finally, the data returned from the mission can be used to validate and update existing spacecraft shielding models as well as Jovian radiation environment models. The radiation data collected can be a resource to enhance our scientific understanding of the global Jovian magnetosphere and the local radiation environment in the vicinity of Europa.

It is widely known that Jupiter is a host to the most intense radiation belts yet observed in the solar system (e.g., Bolton et al. 2004). The magnetosphere of Jupiter is remarkably different from that of the Earth, and its intense radiation environment likely results from several factors: First, Jupiter possesses the strongest magnetic field in the solar system with a magnetic moment ∼20,000 times stronger than the Earth's. As the magnetic field at the equator is proportional to the magnetic moment divided by the cube of the radial distance when the distance is expressed in the respective planetary radius, correspondingly, Jupiter's magnetic field is about 20 times stronger than that of Earth. In addition, the environment is enhanced by large amounts (∼1000 kg/s) of sulfur and oxygen ions that are continuously supplied by Io's volcanic activity (Lopes-Gautier et al. 1999; Russell et al. 2001). Finally, Jupiter's rapid rotation (10 hour versus 24 hour for Earth) shields the inner magnetosphere from the fields carried by the solar wind (but see Murakami et al. 2016) and disturbances in that plasma (Carbary 1980; Paranicas et al. 1991; Khurana 1992, 1997; Khurana and Schwarzl 2005). Figure 1 is a schematic representation of the Jovian magnetosphere. Pronounced wave-like variations in the high energy particle fluxes led to the idea that the Jovian magnetosphere is distorted into a thin disk or plasma sheet (Dessler 1983) – and that this thin disk is populated by a cold plasma consisting of heavy ions originating from Io.

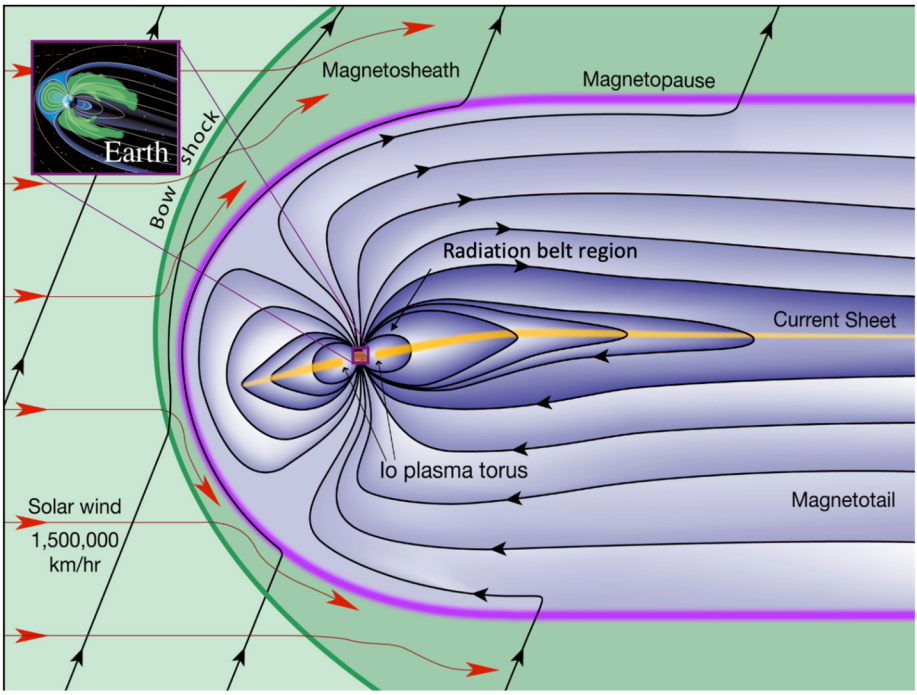

Fig. 1 Schematic representation of Jupiter's magnetosphere illustrating the various plasma regions and particle flows (Credit: University of Colorado, Laboratory of Atmosphere and Space Physics). The Europa Clipper mission will spend most of its time in the equatorial plasma sheet region

Another feature of the Jovian magnetosphere is that the energy spectrum of the trapped electrons in Jupiter's radiation environment extends to much higher energies than do the spectra at other planets (Bolton et al. 2002; de Pater and Dunn 2003). In other words, the fluxes of electrons do not fall off as sharply with increasing energy as, for example, at the Earth or Saturn (Jun and Garrett 2005; Jun et al. 2019b). Instead, the flux energy spectrum decreases more gradually with increasing energy. This makes it much more difficult to shield instrumentation and electronics for missions visiting the Jovian environment. Electrons have much longer path lengths into materials than protons and heavy ions of the same energy, due to their much smaller mass. When high-energy electrons impact materials, they slow down and, in the process, create secondary electrons and energetic photons (i.e., bremsstrahlung). These secondary photons can reach much deeper into the material since their absorption cross-sections are much smaller than those of electrons. Significantly, based on Galileo Near-Infrared Mapping Spectrometer (NIMS) data, the γ-rays produced by energetic electron bremsstrahlung within shielding have been shown to be at least as significant as the primary radiation flux (Carlson and Hand 2015). These γ-rays are also very hard for additional shielding to mitigate.

The radiation belts of Jupiter have been explored by many spacecraft during flybys of the planet (Pioneers 10 and 11, Voyagers 1 and 2, Ulysses, New Horizons, and Cassini) and with orbiters (Galileo and Juno). Although the Jovian system has been visited many times, understanding the characteristics of the radiation environment and magnetosphere still remains a scientifically interesting subject that requires more comprehensive spatial and temporal measurements of low- and high-energy electrons and ions. Especially, characterization of the

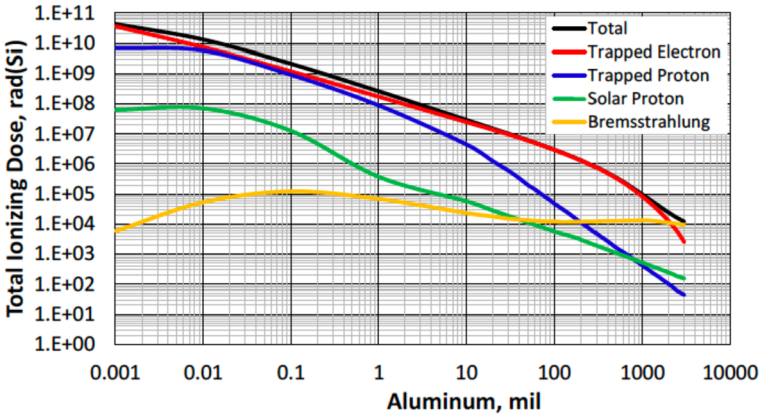

Fig. 2 Total ionizing dose-depth curve, with dose as a function of the thickness of a spherical shield of aluminum for the Europa Clipper design reference mission without any safety factor added. For reference, 1,000 mil = 1 inch = 2.54 cm

very high range of the energy spectrum has been lacking for electrons above ∼1 MeV because direct measurements of these particles are very difficult. These high-energy electrons can deeply penetrate materials and only lose a fraction of their energy, so their quantitative measurement becomes difficult. Europa Clipper will orbit Jupiter at distances in the range of ∼9−50 Rj and conduct multiple (∼50) flybys of Europa. The elliptical and equatorial orbits of the spacecraft under the Europa Clipper mission will be similar to those of the Galileo mission. However, the mission will offer an excellent opportunity to improve our knowledge of the Jovian radiation environment and magnetosphere, and the environment near Europa. Further, the Europa Clipper observations will provide better temporal and spatial coverage than previous missions. The acquired radiation data may allow the determination of the long-term variability of the radiation environment between the Galileo, Juno, and Europa Clipper mission eras. Furthermore, the European Space Agency's (ESA's) JUpiter ICy moons Explorer (JUICE) spacecraft (Grasset et al. 2013) may venture into the Jovian magnetosphere in the same timeframe as the Europa Clipper, which could provide an opportunity to perform synergistic two-point measurements within the Jovian magnetosphere.

Preliminary modeling shows that the RadMon and the other instruments are most responsive to electrons with energies >1 MeV. This finding is corroborated with the mission dose-depth curve as shown in Fig. 2. The TID is dominated by trapped electrons passing through aluminum shielding up to >2.54 cm in thickness. Hence, we devote the majority of the discussions herein to the high-energy electron environment and our current understanding of the potential science that can be achieved with these data. However, for completeness, we also include a brief overview of other constituents of Jupiter's magnetospheric environment (e.g., plasma, high-energy ions).

This paper is structured as follows. Section 2 describes the current and general understanding of the Jovian radiation environment resulting from past flight observations and modeling efforts. That section concludes with a brief summary of the outstanding questions that remain for the Jovian radiation and magnetospheric science communities. Section 3 provides a summary of RadMon's measurement objectives, which is followed in Sect. 4 by a more detailed description of the RadMon hardware and its measurement capability. Section 5 then presents a synopsis of radiation data that can potentially be obtained from other science payload instruments. Potential science questions that could be answered by the Eu-

Table 1 Structure of Sect. 2.1 – Data and models available

	Particle Type	Section
Data	High energy electrons/protons	2.2.1
	Plasma	2.2.2
	Ground base – Synchrotron	2.2.3
Models	Empirical: GIRE and JOSE(*)	2.2.4
	Theoretical	2.2.5
	Plasma at Europa	2.2.6

(*) GIRE: Galileo Interim Radiation Environment; JOSE: JOvian Specification Environment

ropa Clipper radiation environment measurements campaign are described in Sect. 6. We conclude the paper with a summary in Sect. 7.

2 Current Understanding of the Jovian Radiation Environment and Outstanding Questions

This section provides an overview of radiation data sources available from the past and current Jovian flight missions along with empirical radiation belt models developed based on those data. We do not attempt to provide a comprehensive review of the data and models available. Rather, references are given when and where appropriate. The goal is to provide a survey of current research and Europa Clipper's anticipated contribution to improve the state of the art. In addition, the radiation environment in the vicinity of Europa is presented based on our current understanding. We close the section with the open questions of the Jovian radiation environment and magnetosphere. In Sect. 6, we present how the monitoring of Europa Clipper's radiation environment can help address some of these knowledge gaps.

2.1 Available Data and Models

Table 1 has been prepared to guide the discussion in this subsection about the radiation data and belt models currently available.

2.1.1 Available Data: High Energy Particles

In-situ particle data are available from several flyby missions (Pioneer 10 and 11, Voyager 1 and 2, Cassini, Ulysses, and New Horizons) as well as orbiter missions (Galileo and Juno). As can be easily inferred, the flyby missions have only provided snapshots of the Jovian environment at the times of their flybys. The most comprehensive sets of energetic particle measurements were provided by the Energetic Particle Detector (EPD) of the Low-Energy Magnetospheric Measurements System (LEMMS) instrument onboard the Galileo orbiter. The available high-energy radiation data (particle species, energy range, and temporal and spatial coverages) from these flyby and orbiter missions are well summarized and reviewed in Divine and Garrett (1983) and Sicard-Piet et al. (2009). These references provide a holistic summary of the available radiation data from previous missions. More recently, the EPD/LEMMS high-energy particle data have been re-analyzed and reported in Garrett and Jun (2021) and Kollmann et al. (2020). For the case of high energy electrons, the EPD/LEMMS nominally provides coarse integral measurements up to >11 MeV. Besides

using the original design features of instruments, it has been shown that the Galileo star scanner can provide a proxy for the >11 MeV electrons (Jun et al. 2019a; Fieseler 2000). Note that the EPD high-energy proton data are generally considered to be contaminated by electrons, and only the proton data from the B0 channel are valid (Jun et al. 2002).

The ongoing Juno mission also measures the radiation environment at Jupiter (Becker et al. 2017). For example, the JEDI instrument (Mauk et al. 2018) provides energy-resolved differential intensities of electrons in the range from 20 keV to 700−1000 keV. Furthermore, although not designed to measure high-energy particles, Juno is able to measure opportunistic high-energy electrons. For example, the Juno Ultraviolet Spectrograph (UVS) (Gladstone et al. 2017) was shown to be sensitive to >6 MeV electrons that penetrate its tantalum shielding (Zhu et al. 2021) although Juno-UVS is primarily designed to observe auroral H and H_2 photon emissions at wavelengths between 68 and 210 nm. These electrons interact with the microchannel plate (MCP) detector, producing a time series of events mixed in with detections of UV photons. During periods of intense radiation, the count rate associated with this interaction dominates the UV photon counts, and these excess count rates can be interpreted as the signature of high-energy electrons. Similarly, it was demonstrated (Steffl et al. 2013; Kammer et al. 2018) that the UVS data can be used to investigate the Jovian radiation environment with the New Horizons ALICE instrument (Stern et al. 2008), which measured current sheet properties as a complement to the Pluto Energetic Particle Spectrometer Science Investigation (PEPSSI) energetic particle measurements during its Jupiter gravity assist flyby, at >32.2 Rj. To summarize, the Juno mission can constrain >1 MeV (Mauk et al. 2018; Zhu et al. 2021) and >15 MeV electrons (Mauk et al. 2017; Paranicas et al. 2018b) using JEDI observations, and >6 MeV electrons using UVS data (Zhu et al. 2021). Juno flew by Ganymede in June 2021 and Europa in September 2022. Io flybys are also planned in 2023 and 2024. The radiation environment measured during the Ganymede flyby is reported in Paranicas et al. (2021).

The Galileo and Juno datasets are complementary to each other, with those from the Galileo mission sampling the equatorial plane and Juno the high latitudes. However, both data sets only provide limited information on the directional distribution of the electrons, which bears information on source regions and acceleration processes (Tomás et al. 2004; Mauk et al. 2020). Unfortunately, Galileo data acquisition was limited due to its low available data rate and provided high resolution only occasionally. Consequently, most Galileo data have a low time resolution, which obscures small-scale structures such as the moon micro-signatures (Andriopoulou et al. 2012). Juno generally does have good coverage and resolution of local pitch angles, but it cannot access particles that do not bounce up to the spacecraft. This is because particles mirroring below Juno's magnetic latitude, which is dependent on the particle pitch angle, cannot be sampled by Juno. The pitch angle is defined as the angle between the magnetic field and the particle's velocity vector. For example, the particles with a pitch angle of 90° at the magnetic equator are confined in the magnetic equator (so-called locally mirroring). At the Juno spacecraft location, only particles with pitch angles greater than a certain value, which is dependent on the local magnetic field strength, can be measured. This means that Juno, exploring the high latitude regions, cannot sample the entire magnetospheric environment. Due to the relatively large amount of data provided by the orbiters, measurements from the flyby missions are generally less useful, except for some measurements provided by their unique instrumentation. For example, measurements of energetic electrons, characterized with energies >31 MeV, have been made by Pioneer 10 and 11 (Nénon et al. 2017).

2.1.2 Available Data: Plasma

The plasma environment at Europa's orbit was measured by a variety of instruments on the Voyager and Galileo spacecraft. The PLasma Spectrometers (PLS) aboard each spacecraft measured energy spectra of ions and electrons less than 6 keV on Voyager and 52 keV on Galileo. For both missions, the signal was dominated by particles with energies of about 1 keV, the approximate corotation energy of sulfur and oxygen ions. The electron density was also measured using the frequency of the upper hybrid emission observed by Voyager's Planetary Radio Astronomy (PRA) and Galileo's Plasma Wave Spectrometer (PWS).

A comprehensive review of the PLS ion data from the PDS archive has been presented by several researchers (e.g., Bagenal and Delamere 2011; Bagenal et al. 2016). More specifically, these works entail fitting the ion distribution functions in terms of V_r (ion bulk radial velocity), V_θ (ion bulk velocity in latitudinal direction), V_ϕ (ion bulk velocity in the azimuthal direction), ion temperature, ion total density, and the uncertainties in these parameters. The data analysis covered the entire Galileo mission at Jupiter for radial distances between 5 Rj and 30 Rj. The main data source for the plasma environment modelling in the spatial range 8−10 Rj has been the two Voyager PLS experiments for particle energies <5 keV. Details of the original Voyager PLS data analysis are presented in terms of total moment densities and temperatures (Sittler and Strobel 1987). More recently, the Galileo PLS electron data have been re-analyzed to remove the apparent contamination, especially between 8 and 10 Rj, by high energy electrons (Jun et al. 2019b).

The Jovian Auroral Distributions Experiment (JADE) instrument on the Juno mission measures ion and electron fluxes over energy ranges that have varied during the mission. Subsets of these measurements have been converted to plasma moments for different ion species, even species with the same mass-to-charge ratio (m/Q) (e.g., Kim et al. 2020). We expect that these plasma moments will become available in the future.

2.1.3 Available Data: Ground Based Observations – Synchrotron

Since the 1950s, it has been shown that the nonthermal decimetric radio emissions with wavelengths between 22 cm and 68 cm obtained from ground-based observations are due to synchrotron radiation from relativistic electrons trapped in the Jovian magnetic field – the radiation belt (Drake and Hvatum 1959). Since then, synchrotron radio emission from Jupiter observed from the Earth has been an important tool for understanding the magnetic field and relativistic electron population in Jupiter's inner (1.2 to 3.5 Rj) magnetosphere. High-resolution radio maps of the synchrotron emission made with the Very Large Array (VLA) and other antenna arrays including Australia Telescope Compact Array (ATCA) have provided a wealth of information on the emission (Leblanc et al. 1997; Dulk et al. 1999; de Pater and Dunn 2003) These synchrotron data have been also used to update the Jovian radiation belt model (Garrett et al. 2005). In order to assess the radiation hazard to the Pioneer spacecraft, crude numerical models of the energetic electrons and protons were developed based on these observations (see summary by Beck 1972). Modern examples include the physics-based Salammbô model (Sect. 2.1.5) as well as the Divine family empirical model called GIRE (Sect. 2.1.4). Figure 3 shows ground-based measurements of this Jovian synchrotron radiation at 1400 MHz (Fig. 3A) and the corresponding model predictions (Fig. 3B).

2.1.4 Radiation Belt Models: Empirical

Jupiter's magnetosphere has been known to contain radiation belts since, in analogy with early spacecraft observations of the Earth's radiation belts, it was realized that the Jovian

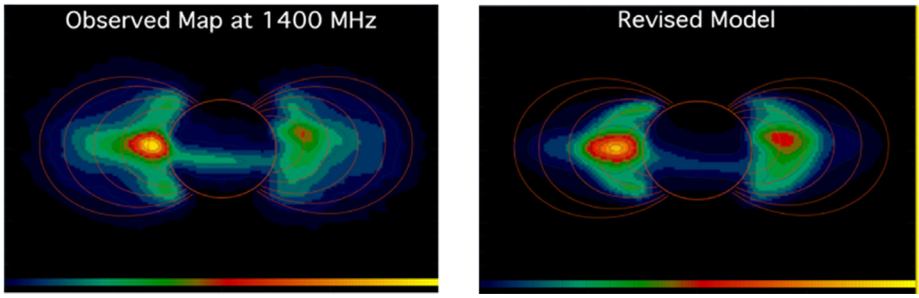

Fig. 3 A) Earth-based observations of Jovian synchrotron radiation at 1400 Mhz. B) Simulated Jovian synchrotron radiation at 1400 Mhz using the Divine family of Jovian electron radiation models (Garrett et al. 2005)

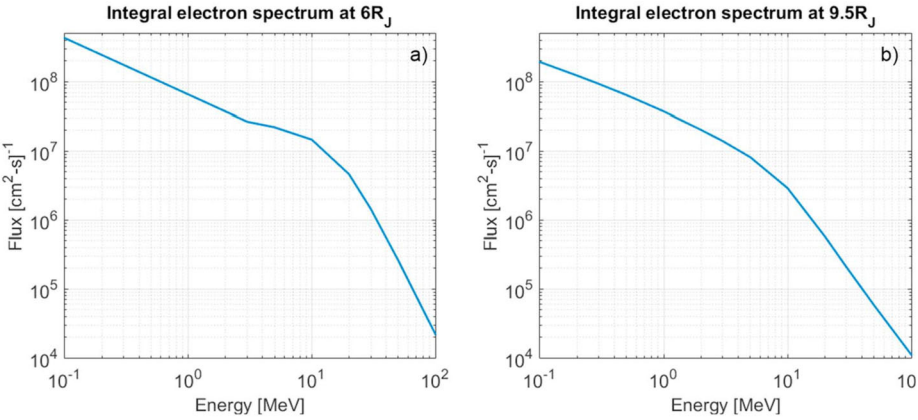

Fig. 4 Integral electron spectra at (a) 6 Rj and (b) 9.5 Rj as given by the GIRE3 model. A comparison of electron flux between GIRE3 and JOSE as a function of Rj is also shown in (Soria-Santacruz et al. 2016)

UHF radio emissions could be interpreted in terms of trapped energetic electrons (Drake and Hvatum 1959). The passage of Jupiter by Voyagers 1 and 2 further refined the particles and fields observations. The Galileo orbiter mission has further improved our understanding of the Jovian radiation environment based on the rich dataset collected over the ∼7-year mission. Theoretical models have also guided the interpretation of the observations and have led to the development of Jovian radiation models capable of making practical predictions about the environment around Jupiter. To date, the principal models of the Jovian radiation belt are the Divine family of models (Divine and Garrett 1983; Jun et al. 2005a; Soria-Santacruz et al. 2016; Garrett et al. 2017) mainly developed by JPL and the JOSE model (Sicard-Piet et al. 2011) developed in Europe. Note that JPL's electron environment model is described in Soria-Santacruz et al. (2016), and JPL's proton and heavy ion model is described in Garrett et al. (2017). This composite model for electrons, protons, and heavy ions is called Galileo Interim Electron Environment (GIRE). The latest model is version 3 (GIRE3). Figure 4 shows examples of electron energy spectra at 6 Rj (Io's orbit) and 9.5 Rj (Europa's orbit) estimated using the GIRE3 model. There are also several publications

of the average intensities and their variation, even though they do not attempt to provide continuous numerical values over various dimensions (e.g., Kollmann et al. 2021, 2018).

There are several detailed magnetic field models of Jupiter. One such example is the Voyager-Io-Pioneer fourth degree order interior magnetic field model (as such, it is named VIP4) (Connerney et al. 1998) in combination with the external current sheet model by Connerney et al. (1981). The latter current sheet model accounts for the effects that arise from the pronounced Jovian plasma sheet and its distortion of the magnetic field inside of $L = \sim 20$. Outside of $L = \sim 16-20$, a more recent magnetic field model has been developed by Khurana and Schwarzl (2005) to model the magnetic field of the outer plasma sheet. The internal dipole is offset about 0.1 Rj and tilted about 10°, and its polarity is opposite of the fields of Saturn and the Earth. Recently, a magnetic field model has been developed from Juno observations (Connerney et al. 2020), which uses an internal field model called the Juno Reference Model through Perijove 9 (JRM9, Connerney et al. 2018). It is worthwhile to note that the external magnetic field model is usually linked with the choice of the internal magnetic field model being used.

2.1.5 Radiation Belt Models: Theoretical

In addition to the empirical models described in the preceding section, a theoretical model exists that is based on the Salammbô model for the Earth's radiation belts (Beutier and Boscher 1995) and that has been adapted for Jupiter (Nénon et al. 2017; Sicard and Bourdarie 2004). This model has been validated for protons and electrons for radial distances from $L = \sim 1$ up to the orbit of Europa. The motions of trapped electrons are solved via a diffusion equation in which various physical processes (such as interaction with moons/dust, wave-particle interaction, synchrotron radiation, and radial diffusion) are represented by distinct diffusion coefficients.

The spatial range of the model extends from $L = \sim 1$ to $L = 9.5$ for electrons, and the electron energy covers the range between 1 and 100 MeV. In order to have a more accurate picture of the radiation belts outside Io's orbit, the O6 model (Connerney 1993) is used to describe the internal magnetic field. The O6 model uses a spherical harmonic expansion of the planetary field to degree 3 and order 6. In addition, an external field model by Khurana is used to provide more realistic field lines at large distances from the planet (Khurana 1992, 1997).

2.1.6 Radiation Belt Models: Plasma Environment at Europa

While we have discussed the energetic particle ($> \sim 1$ MeV) environment at Jupiter's magnetosphere in this section, here we discuss the currently available representative low-energy plasma environment (typically $< \sim 100$ keV) models at Europa. A representative plasma environment spectrum at the Europa orbit is shown in Jun et al. (2019a) based on the reanalysis of Voyager and Galileo PLS data.

Europa possesses a tenuous atmosphere that interacts electrodynamically with Jupiter's magnetosphere through various mass-loading processes. This interaction inevitably modifies the incident Jovian plasma flow around Europa and perturbs the magnetic field in the vicinity of the moon (Jia et al. 2010). Much of the interaction physics can be understood in the context of the so-called "Alfvén Wing" model (Jia et al. 2010), which considers the formation and propagation of different wave modes in a magnetohydrodynamic (MHD) plasma (Neubauer 1980, 1998; Southwood et al. 1980). In addition, several numerical simulations based on MHD or hybrid approach have been developed, which provide insights into the

three-dimensional structure and variability of Europa's interaction with the Jovian magnetosphere. In MHD simulations, both electrons and ions are treated as fluids while in hybrid simulations, ion motion is considered to be kinetic and only electrons are treated as a fluid.

Saur et al. (1998) developed a plasma model to consider the interaction between the Jovian magnetospheric plasma and Europa's atmosphere while also considering various source and loss processes important for the atmosphere. Their results demonstrate that Europa's atmosphere and the magnetospheric plasma are strongly coupled and influence each other. Schilling et al. (2008) used a single-fluid MHD model to investigate the influence of the magnetic field induced within Europa's subsurface ocean on the plasma interaction. Their model results suggest that the induced field causes deformation and displacement of the Alfvén wings, in agreement with previous theoretical predictions (Neubauer 1999) as well as the Galileo spacecraft data (Volwerk et al. 2007). Recently, Rubin et al. (2015) and Harris et al. (2021) have employed a multi-fluid MHD approach to simulate Europa's plasma interaction, where ions originating from Jupiter's magnetosphere and those from Europa are tracked as separate plasma fluids while the coupling among different fluids and their interactions with Europa's atmosphere through collisional effects are also modeled self-consistently. The separate treatment of distinct ion species allows for a more accurate assessment of the perturbations to the incident Jovian plasma flow around Europa resulting from the electrodynamic interaction. Using the multi-fluid MHD model, Harris et al. (2021) investigated how the large-scale configuration of Europa's plasma interaction responds to the variability of the external plasma and field conditions. They found that a significant fraction of the incident Jovian flow is diverted around Europa due to the plasma interaction, resulting in much-reduced access of Jupiter's magnetospheric plasma to Europa's surface.

Recent modeling efforts have been focused on characterizing the effects of atmospheric inhomogeneities or plumes on the plasma and magnetic environment around Europa (e.g., (Blöcker et al. 2016; Jia et al. 2018; Arnold et al. 2020) The results from this modeling work not only reveal the complexity of Europa's plasma interaction, but also provide valuable context for interpreting future observations, such as those that will be obtained by the Europa Clipper.

It is worth noting that the present plasma interaction simulations, whether MHD-based or hybrid models, do not directly model energetic particles (e.g., >1 MeV), which are the main constituent of the radiation environment at Europa. However, the electromagnetic fields output from those physics-based models can be used to drive test particle simulations, which in turn provide insight into the behavior of energetic particles in the near-Europa space environment. For example, these simulations can be used to quantify particle access to Europa's surface, which influences the weathering of the surface (Breer et al. 2019; Nordheim et al. 2022).

2.2 Radiation Environment at Europa's Surface

Understanding the radiation environment at Europa's surface is central to informing several scientific investigations and thereby improving our understanding of Europa's habitability. For example, radiolysis and sputtering modify the surface composition, contribute to the exospheric environment, and may ultimately influence the inventory of reductants and oxidants in the ocean itself (Hand et al. 2009). All of these factors make radiation especially important to a potential future Europa lander designed to search for biosignatures (National Research Council 2002; Hand et al. 2022). However, characterizing the surface radiation environment is complicated mainly because the environment around Europa is perturbed by the presence of Europa itself, which is embedded deep within the Jovian magnetosphere. The dynamics

of particles (high energy versus low energy versus electrons or ions) in the vicinity of Europa are modified by the induced magnetic field originating from the interaction between the time-varying Jovian magnetic field and the conductive subsurface ocean. The motion of the particles is further complicated by the interaction of the moon with Jupiter's thermal, corotating magnetospheric plasma. As Europa's orbital period (∼85 h) is substantially larger than Jupiter's synodic rotation period (∼11.2 h), the moon is continuously overtaken by partially corotating plasma at a relative velocity of about 100 km/s (Kivelson et al. 2009). The plasma current arises because electrons and ions are corotating in the opposite direction. Another major contribution to these plasma currents arises from the interaction between the magnetospheric flow and Europa's dilute, sputtering-generated atmosphere (e.g., Saur et al. 1998; Rubin et al. 2015).

There have been many studies to investigate particle dynamics around Europa and its precipitation patterns on the surface. The most complete method to compute particle precipitation is to follow individual particle trajectories. Paranicas et al. (2001, 2007) and Nordheim et al. (2018) used the facts of small electron gyroradius and rapid bounce to estimate the precipitation patterns on Europa. This oversimplifies the particle motion and any effects due to a finite gyroradius would likely be missed. More recent studies of magnetospheric ions started to include a more complex particle tracing algorithm to account for realistic (i.e., perturbed) local magnetic field configurations near Europa (e.g., see Breer et al. (2019) for ion impact to Europa). However, electron dynamics under the influence of a perturbed magnetic field and the mapping of electron precipitation map onto the surface have yet to be addressed. Nevertheless, it is clear from previous studies that strong asymmetries exist in the radiation incident maps between leading and trailing hemispheres, especially for electrons, and knowledge of the perturbed magnetic field is important for better constraining a particle's motion around, and onto, Europa. In addition, we note that, to date, the characterization of the surface environment has been model-dependent because in-situ measurements have not yet been performed at the surface. However, the flux reduction signatures observed in the Galileo EPD data confirm that the hemispheric asymmetry is a real phenomenon.

2.3 Open Questions

While our understanding of the Jovian radiation environment and the local environment at or near Europa has advanced in many aspects over the last two decades through careful analyses of Galileo and Juno data and modeling efforts, there are still many physical phenomena that need to be addressed. We anticipate that the Europa Clipper mission can provide additional observational clues to help improve our understanding of the following topics:

- Long-term variation of energetic charged particles: For example, the high-energy electron data from the Galileo EPD showed the >1 order of magnitude orbit-to-orbit variability of the trapped electron environment over the seven year mission lifetime (Jun et al. 2005b). Observation of high-energy electrons in the longer term would be an interesting observation that might shed light on the long-term stability or dynamics of the trapped electrons.
- Magnetic local time dependence: Galileo revealed that the plasma environment at Jupiter showed local time asymmetries, suggesting that the solar wind quite likely drives a convection system in Jupiter's magnetosphere (Khurana et al. 2004). However, the local time variability of high-energy trapped electrons has not been studied extensively.
- Ultra-high-energy electron population and physical mechanism for energization: Electrons with energies >10 MeV at Jupiter have been of great interest to scientists seeking to understand the universal process of particle acceleration, as well as for mission planners attempting to estimate spacecraft radiation effects. However, it has been difficult to infer

energy-resolved spectra for electrons at energies of ∼10 MeV or higher from observations by previous missions.

- The physical mechanism for stormtime enhancements: According to the Galileo EPD data, there were several periods during the mission when enhanced electron fluxes were observed (Jun et al. 2005b). Among these, the Callisto flyby orbit #22 (C22) showed the most pronounced enhancement. Physical mechanisms for this storm-like environment enhancement are not yet understood (e.g., see Hao et al. 2020).
- Depletion of electron fluxes and its energy dependence near Europa (leading versus trailing hemisphere): The current understanding of the near-Europa environment is mostly based on an analysis using a simple guiding center approximation of the particle motion. While this is observationally corroborated by the Galileo EPD data (e.g., Paranicas et al. 2000), more observations are needed to better constrain the relationship between the energetic electron environment and surface features (e.g., Patterson et al. (2012)).
- Dynamics of electron flux in the perturbed magnetic field configuration around Europa: Europa is embedded in Jupiter's magnetospheres. Sources of variability to the plasma and fields include the location of the subsolar point, Europa's magnetic latitude and inductive response, the Alfvén wing currents, and changes in the plasma flow, density, and temperature. Currently, the motion of energetic electrons in this perturbed electromagnetic environment is not well studied. More observation would be desired to help the model development.
- Additional science enabled by the Europa Clipper radiation data include the study of the roles of energetic electrons on surface chemistry/physics (e.g., sputtering) and extracting details of the interaction between Europa and the planet and magnetosphere.

3 Radiation Monitor Measurement Objectives

3.1 Engineering Resource for Spacecraft Threat Assessment

The RadMon serves as an engineering resource for the Europa Clipper mission. RadMon is optimized to measure those radiation effects that pose the most significant threats to the health and safety of the spacecraft in the challenging radiation environment near Europa. From Fig. 2, contributions to the ionizing radiation environment from electrons are expected to dominate those from protons by roughly two orders of magnitude over equivalent shielding levels of 100 mil to 1000 mil of aluminum, which is a range of shielding most relevant to spacecraft electronics assemblies. RadMon will provide two sets of electron-focused measurements that are vital to assessing the impact of Europa's radiation environment on the spacecraft: The Total Ionizing Dose (TID; Sect. 3.2) leads to gradual electronic component failure, and the charging of the spacecraft by energetic electrons may lead to Internal Electrostatic Discharge events (IESD; Sect. 3.3). This section provides a description of the planned measurements by the RadMon to assess the radiation exposure of the spacecraft. Details of radiation effects on the instruments and impacts to their measurements and operations in Jupiter's harsh radiation environment (e.g., noise level derivation, instrument operations, flyby configuration, optimized instrument setting) can be found in each instrument paper in this collection.

3.2 Measuring Total Ionizing Dose

TID is a cumulative effect in which ionization processes from radiation degrade spacecraft electronics' performance over the life of the mission. Mitigating these effects was a driving environmental factor for the design of all electronics assemblies across the spacecraft.

Owing to its position within the Jovian magnetosphere, the environment near Europa is particularly challenging from a TID perspective. Electronics component options for the mission were significantly limited due to the stringent selection criteria for radiation susceptibility. In general, TID is expected to be a dominant wear mechanism for a majority of spacecraft electronics assemblies. Given the concerns regarding TID effects, characterization of accumulated TID over the course of the mission is important both as a verification for the expected dose obtained from modeling, as well as a predictor of future dose for the remainder of the mission. In addition, as the mission progresses, accumulated TID measurements will be one factor used to assess the spacecraft's degradation over time. Characterization of this aging through spacecraft housekeeping data as well as correlation with direct measurements and models of the TID will help inform mission decisions about operational constraints or the duration of possible extended missions – perhaps allowing the mission to treat TID as a consumable when comparing different mission design options.

3.3 Measuring Electron Environment

In addition to TID, spacecraft charging, primarily due to impingement by energetic electrons to spacecraft, poses a particular hazard to the mission. While charging is a typical concern for all spacecraft with dielectric materials and ungrounded metals, penetrating electrons near Europa are intense and can result in significant charge accumulation not just on the spacecraft surface but within the body of the spacecraft. When sufficient charges accumulate, an IESD event may occur. The resulting voltage spike can cause temporary disruption or permanent damage to spacecraft electronics, including instruments, and may affect the ability to perform science observations. It is not realistic to measure these discharges directly, because they may occur anywhere in the spacecraft. However, the RadMon does measure charging rates across several broad energy ranges to characterize the fluctuation in the energetic electron flux over time. With these data, spacecraft anomalies such as component-level resets can be correlated with the RadMon charging data to assess whether these anomalies were likely to be the result of IESD events.

Finally, because the majority of accumulated TID is also from energetic electrons, the two measurements are complementary rather than redundant. The TID increases slowly over the life of the mission and is manifested in the degradation of electronics' performance. In contrast, the charging measurements are more direct and represent a real-time characterization of the electron environment. The two types of measurements offer the opportunity for cross-calibration. The electron flux will peak during Europa flybys, and it should be possible to correlate the rate of change of the TID measurement with the electron charging measurement. Consequently, the electron charging data should provide a means of improving the accuracy of the coarser TID measurements.

4 Radiation Monitor for the Europa Clipper Mission

4.1 RadMon Components Overview

The Europa Clipper's RadMon subsystem consists of multiple elements. The primary assembly is the main "sensor assembly," which hosts a Charge Rate Monitor (CRM) to measure the net charged particle environment at multiple penetrating depths (see Sect. 4.4). In addition, the sensor assembly performs TID measurements at multiple shielding depths in the TID stack assembly. This and all other TID measurements are based on a common sensor,

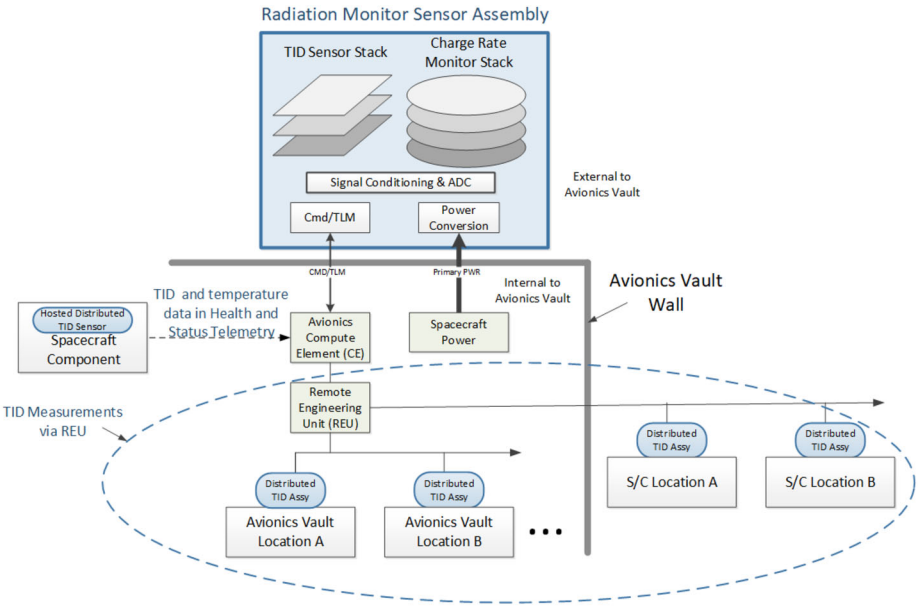

Fig. 5 Radiation Monitoring subsystem block diagram showing the connectivity of its elements. The Sensor Assembly communicates directly with the Avionics Compute Element, while the DTID's are read by the Remote Engineering Unit (REU). Hosted TID sensors are read by their respective host subsystem/instrument (PIMS, UVS, or avionics)

the hybrid RadFET, and are discussed in Sect. 4.3. Additional sensor assembly TID measurements are taken by hybrid RadFETs on the sensor assembly's common electronics unit (CEU) and measurement boards.

The RadMon operation is not critical to spacecraft survival, and therefore the sensor assembly, and particularly the charging measurements, are not redundant. This means that the RadMon is not redundantly designed in the event of a single point failure related to this subsystem. However, multiple TID measurements are acquired by eight small Distributed TID assemblies (DTIDs, Sect. 4.3) and collected by the avionics Remote Engineering Unit (REU).

A third source of TID measurements are the nine "hosted" TID RadFET dosimeter sensors (Sect. 4.3) located on electronics boards in two instruments (PIMS and Europa-UVS) and the spacecraft avionics vault, which have their data reported in the hosting component's housekeeping telemetry. The sensor assembly, DTID, and hosted RadFET measurements are each collected independently, and subsequently combined for joint analysis after transmission to the ground. The total doses expected for the distributed sensors range from 250 krad to 35 krad, which corresponds to the effective aluminum shielding of 600 mil (or 4.11 g/cm^2) to 1600 mil (or 11 g/cm^2) per Fig. 2. The shielding levels for the RadFETs in the sensor assembly are described in Sect. 4.3.

A block diagram detailing the configuration of the various RadMon subsystem elements is shown in Fig. 5. Although there are three sources of TID data (sensor assembly, DTIDs, and hosted TID sensors), the sensor assembly only controls its own TID measurements. All other TID measurements are recorded independently either by the REU or the hosting spacecraft component. The readout mechanism is identical for all TID measurements in that a 1 mA current is applied to the device, and the resulting voltage across the device is

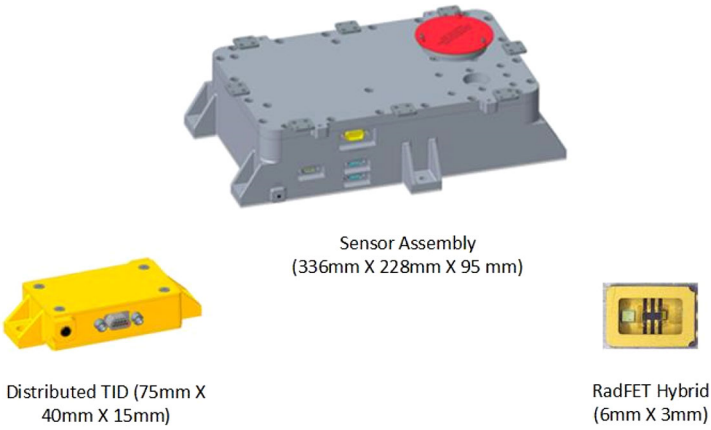

Fig. 6 Illustration of subsystem components. The Sensor Assembly (top center) performs both TID and charge measurements, while the eight smaller DTIDs (lower left) located across the spacecraft measure TID only. The RadFET hybrids (lower right, more detailed view in Fig. 10) function as the TID sensors across the subsystem in both the Sensor Assembly and DTIDs as well as hosted on other electronic boards

measured. It is noted that there are variations in the readout circuit implementation between the various electronics assemblies. The components of the RadMon subsystem including their approximate dimensions are shown in Fig. 6.

Figure 7 shows the locations of the various subsystem elements across the Europa Clipper flight system. The DTID locations were chosen to provide some spatial distribution of TID measurements across the spacecraft, in addition to measurement redundancy. Hosted TID sensors further expand on the variety of locations, but are more opportunistic and depend on the hosting components being able to accommodate them with minimal impact.

4.2 Heritage and Development

The RadMon measurement technique is based on that of the Van Allen Probes Environmental Radiation Monitor (ERM) (Goldsten et al. 2013), which similarly measured TID and charging rates, albeit in an elliptical Earth orbit. Both the Europa Clipper RadMon and ERM use Metal-Oxide-Semiconductor Field Effect Transistors (MOSFETs) for dosimetry (Sect. 4.3) and instantaneous current measurements from charge collection plates for the charging measurement. Both assemblies also conduct multiple TID measurements at varying shielding levels. Shielding variation is also used to provide a coarse energy selectivity for the charging measurements.

The RadMon on Europa Clipper expands on the Van Allen Probes ERM in several ways. The RadMon includes the aforementioned TID sensors at multiple locations throughout the Europa Clipper spacecraft as opposed to a single location for Van Allen Probes. In addition, while the ERM relied upon a primary payload instrument for power and data interfaces, the RadMon sensor assembly accepts spacecraft primary power and has dedicated command and telemetry links to the spacecraft avionics subsystem. To reduce development cost, the RadMon leverages the Common Electronics Unit (CEU) board design that was developed for the PIMS instrument. The CEU includes power conversion, digital logic, and internal housekeeping resources. Although the adaptation of the PIMS hardware created some challenges with respect to packaging, it allowed the development team to focus on radiation

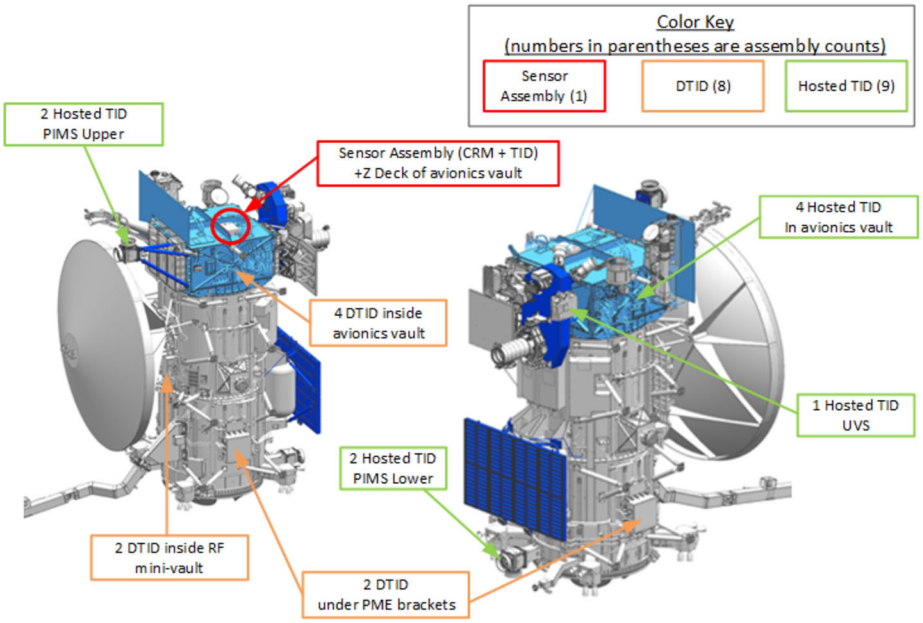

Fig. 7 Subsystem element locations on the spacecraft. The numbers in parenthesis in the Color Key indicate the number of each element on the flight system. The single sensor assembly is located on the avionics +Z deck. It includes 8 RadFETs (3 biased in stack, 3 unbiased in stack, 2 unbiased in CEU) and the CRM. Four DTIDs are located inside the avionics vault, with two DTIDs inside the RF mini-vault and one DTID under each Propulsion Module Electronics (PME) assembly. Hosted TID RadFET hybrids for PIMS, UVS, and avionics are indicated with individual quantities. Unless noted otherwise, the RadFETs are unbiased

measurement electronics. Further efficiencies were achieved in the areas of embedded software and programmable logic design, which substantially leveraged the PIMS design. A view of the sensor assembly's internal structure is shown in Fig. 8, and Fig. 9 shows the flight unit installed on the exterior of the avionics vault +Z panel. Due to the amount of shielding required for both the box walls and the CRM, the sensor assembly mass is 7.7 kg, with a nominal power dissipation of 2.4 W.

The measurement approach is similarly simplified to ease development. All TID sensors provide measurements once per second, and the current from each of the charge collection plates is sampled at the same rate. The measurement data are bundled with housekeeping telemetry from the Sensor Assembly to allow transmission of a single data packet. Although TID measurements will not have detectable variations on the timescale of seconds, our approach is simple and still allows downstream data decimation as dictated by the availability of spacecraft downlink bandwidth and storage. The one-second measurement cadence does not artificially reduce the potential data return of the charging measurement. The responsiveness of the charge measurement is bandwidth limited so that fluctuations in the electron environment faster than one second would be filtered by the electronics. TID measurements not taken by the Sensor Assembly are also reported at one-second intervals by either the hosting instrument/avionics or the REU. The one second measurement cadence both for TID and charging could be useful if there are detectable variations on this timescale during the flybys as various boundaries are crossed in the moon-magnetosphere interaction region. Away from Europa, these high-rate measurements may be of interest for the study of wave-particle interactions leading to electron acceleration and diffusion.

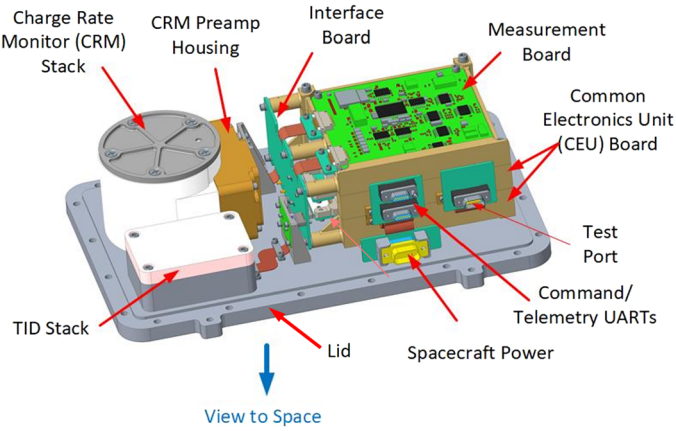

Fig. 8 Illustration of the Sensor Assembly key components. In the shown orientation, the view to space is pointing downward from the lid. In this view, the enclosure on the spacecraft side is removed. Components are mounted to the remaining lid, which is shown in grey at the bottom of the figure. The charging measurement is performed through the CRM in the upper right, and the TID measurement through the TID stack at the lower left. The electronics are at the right. The CEU consists of two printed circuit boards (PCBs) connected by a rigid flex cable and is folded in half when mounted into its frames for integration into the Sensor Assembly. The lower PCB contains the power conversion circuitry while the upper PCB contains the FPGA with embedded processor, command, and telemetry links, as well as housekeeping telemetry support circuitry

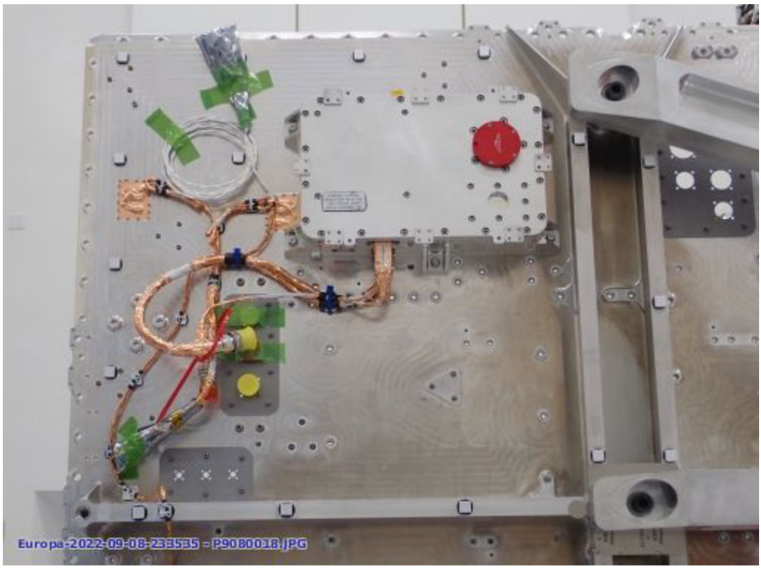

Fig. 9 The Sensor Assembly mounted on avionics vault +Z panel. The red-colored CRM cover will be removed prior to installation of thermal blanketing

Given the relatively low volume of raw data, all measurements are downlinked and analyzed entirely on the ground. No on-board processing occurs, and RadMon data is not used by the spacecraft for autonomy or fault management operations. Ground processing

allows the application of corrections for the TID measurements, as well as aggregation of measurements across different sensors and long-term trending. The ground-processed data could still be used in decisions about commanding the spacecraft and instrument settings for optimal science operations during each flyby. Further details of anticipated data products are provided at the end of this section.

4.3 Total Ionizing Dose Measurement

Dosimetry in the RadMon is accomplished using the well-established technique of measuring the radiation-induced threshold voltage shift in a silicon MOSFET with SiO_2 gate insulators. When used in this manner, the devices are frequently termed RadFETs. In a MOSFET, ionizing radiation generates electron-hole pairs in the device's gate oxide. The resulting holes, which are less mobile than the generated electrons, become trapped and act as recombination centers (e.g., dangling bond point-defects), which increase the effective threshold voltage of the device. Since the amount of trapped charge is proportional to the total ionizing dose received, the threshold voltage change can be used as a measure of TID after calibration of the response with known radiation doses.

Given that the RadFETs are silicon semiconductors, they are good proxies for other semiconductors found throughout the spacecraft, many of which are based on similar technologies. The devices provide a measure of the net effect of ionizing radiation on electronics, are not particularly sensitive to particle species, and satisfy the goal of the RadMon to characterize a significant radiation hazard to the spacecraft.

A TID measurement is acquired by biasing the device with a 1 mA current and reading the resulting voltage across the drain and source terminals. While being read, the device does not accumulate TID in the same manner, which is why the ratio of readout time to TID accumulation time is chosen to be 1% or less.

The devices used in the RadMon are not purpose-built for radiation detection, unlike the devices discussed in Adams and Holmes-Siedle (1978) and Holmes-Siedle et al. (2007). The high TID levels anticipated by the mission would have saturated these more sensitive, dedicated RadFETs. Early in the RadMon's development, a survey of various commercial devices was conducted to identify a MOSFET that would be suitable for the mission. There were a number of constraints. First, there was a strong desire to use a single device for all TID measurements, regardless of the location. Due to the variation in readout electronics, this resulted in a limit in threshold voltage of approximately 2.8 V after a nominal dose of 3000 Gy(Si) (or 300 krad(Si)), which is a key requirement for TID tolerance for the majority of the spacecraft's electronics. Other key considerations were minimizing saturation over dose, as well as linearity of measured voltage over temperature.

Hybrid RadFETs P-channel MOSFET devices were procured in die form and repackaged specifically for the Europa Clipper program in a small ceramic, hermetic package with an Electrostatic Discharge (ESD) suppression diode to protect the gate from damage. The resulting RadFET "hybrids", where hybrid denotes a single package containing multiple integrated circuit die, are shown in Fig. 10. Devices with a well-matched voltage response to a reference input current prior to irradiation show a correspondingly good match in their radiation response. As a result, specific hybrids were selected for the flight from the assembly lot to reduce the range of measured voltages and thereby maximize the uniformity of the radiation response. Hybrid RadFETs are generally used as the basic building blocks for all TID measurements on the mission.

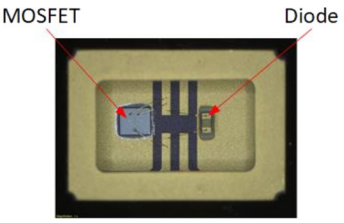

Fig. 10 Hybrid RadFET with lid removed. The radiation-sensing MOSFET die is on the left side of the cavity, and the ESD suppression diode is mounted on the right side

Hosted RADFETs and Distributed TID assemblies Hybrid RadFETs were provided to the host subsystems and instruments as "hosted" RadFETs. The passive, unpowered Distributed TID (DTIDs) assemblies are essentially just a pair of hybrid RadFETs and a pair of temperature sensors in a small housing. Hosted RadFETs, the DTIDs, and sensor assembly RadFETs not within the TID stack have distinct shielding levels (and therefore expected mission TID), which depend on the components location within the subsystem or instrument, and the location of the units within the spacecraft.

TID stack The sensor assembly TID stack was designed to provide multiple shielding environments to use as the TID reference for the mission. Figure 11 shows a cross section of the stack, which has two hybrid RadFETs per shielding level, one unbiased and one biased (see following description). Transport analysis predicts TID levels of 65 krad(Si), 170 krad(Si), and 505 krad(Si) (Radiation Design Factor (RDF) = 1) within the TID stack. For the Europa Clipper mission, these TID values correspond to equivalent spherical shell Al values of approximately 1200 mils, 750 mils, and 400 mils, respectively.

There are some non-idealities inherent in the TID measurement that can be mitigated to improve its accuracy. The gradual decrease in threshold voltage shift (and therefore measured TID) over time is termed "response fade" and results from trapped charge recombination in the oxide layer. Measurements for the RadMon fade are shown in Fig. 12. A simple voltage-to-dose conversion that does not account for response fade would substantially impact the accuracy of the TID measurement if not corrected.

The fade is inversely proportional to gate bias. It can be minimized by placing a voltage bias across the device's gate-source junction (for example, see Holmes-Siedle et al. 2007). Fade is also proportional to temperature. Periods of higher temperature operation affect the rate of fade during subsequent periods of lower temperature. Although temperature variations for the Sensor Assembly are predicted to be less than 20 °C for the planned tour, a customized per-orbit fade correction may still be necessary. The fade rate is further depending on the dose history: The voltage can decrease within days by 10% after an irradiation to hundreds of krad (Fig. 13), while it only changes by 1% within weeks after an irradiation to tens of krad (Fig. 14).

When temperature and approximate dose profiles will be measured along an actual orbit, these conditions can be reproduced on ground, with a well-known dose, which then allows to quantify the fade on ground to be applied to the flight data. Until that data becomes available, a simple correction for the fade occurring between two orbits can be used and is described in Sect. 4.5.1. In addition, while the selected RadFET devices demonstrated generally good sensitivity to radiation, some nonlinearity due to decreased sensitivity at higher radiation doses occurs, especially for unbiased RadFETs. While the nonlinear correction can in principle be handled through calibration, this impacts accuracy at high doses. The nonlinearity of the measurement itself can be reduced by applying a bias voltage, as illustrated in Fig. 15 for the general case and in Fig. 12 for RadMon's flight configuration.

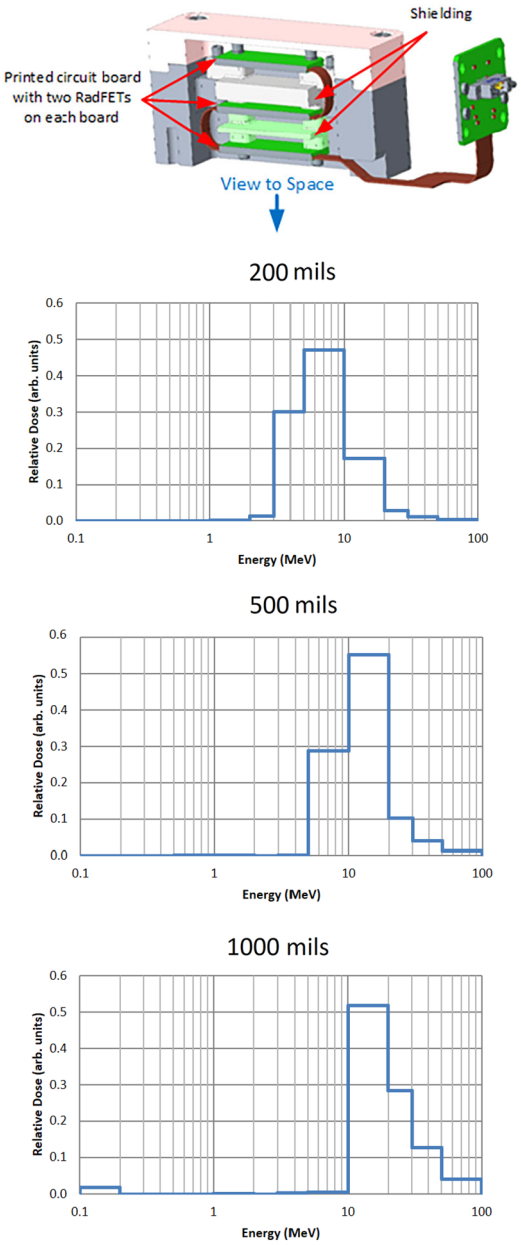

Fig. 11 (A) Upper panel: Geometry of the TID stack consisting of three hybrid RadFETs mounted on green boards and separated by layers of increasing shielding (white and light green). (B) Right panel: Relative response of the RadFETs to electrons of different energies. These simulated responses are based on a model with a 5.6 cm-diameter spherical shell of Al that varies in thickness as shown. The model irradiates a 2 mm diameter silicon sphere in the shell center. The dose is not sensitive to the target dimensions, see Sect. B.2. The simulations demonstrate that the uppermost, least shielded RadFET responds to the lowest energies, with increasing shielding skewing the response toward higher energies. The TID measurement is fairly insensitive to the spectral shape of the trapped electron population. Thus, TID measurements are best suited for forward modeling rather than spectral reconstruction

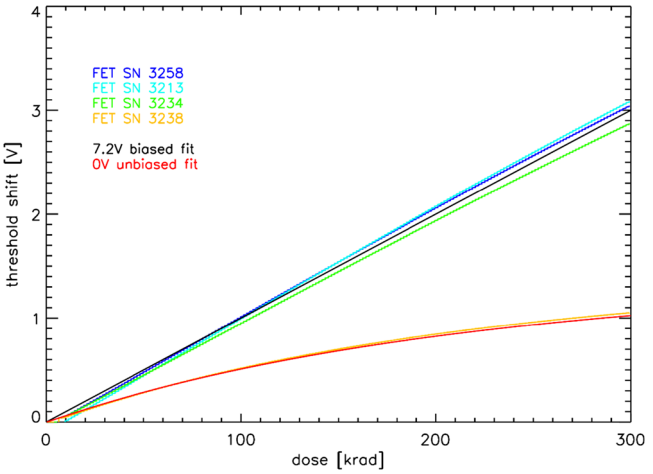

Fig. 12 Dependence of RadFET threshold voltage shift on dose for four RadFETs with the serial numbers given in the legend. Three RadFETs were biased with 7.2 V, while the remaining device was unbiased. Tests were run at 23 °C. The black and red curves show calibration fits with the parameters listed in Appendix A

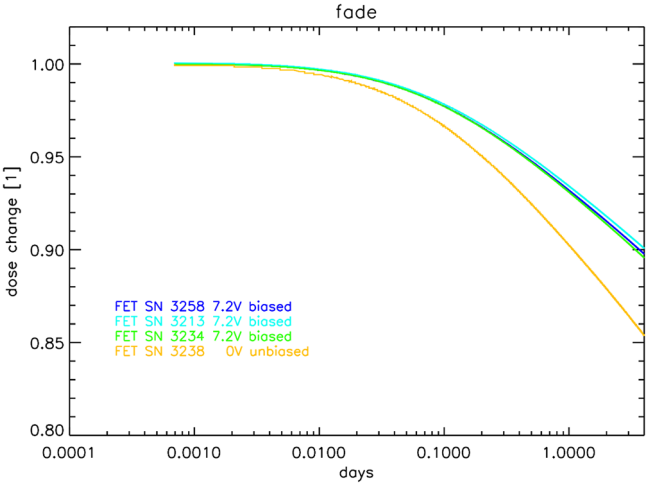

Fig. 13 Relative change in threshold voltage over four days in absence of additional radiation. Data is based on an initial 300 krad dose and uses the same devices shown in Fig. 12. Devices were at room temperature for both initial irradiation and subsequent response measurements

While the bias voltage improves sensitivity and response linearity, and reduces fade, it comes at the cost of more complicated support circuitry. Due to these trades to be considered, RadMon uses the biased configuration only for one RadFET per shielding level in the Sensor Assembly TID stack, while the remainder of the devices in this assembly, the DTID, and the hosted RadFETs are not biased. One reason for using the same device type for all TID measurements is the opportunity for cross-calibration between the biased and unbiased RadFET measurements. The more accurate biased measurements in the sensor assembly can be used as a baseline for correcting nonlinearities in the unbiased responses over time.

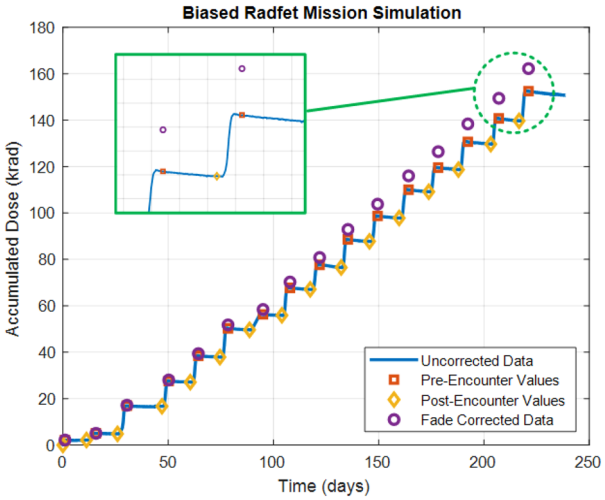

Fig. 14 Fade correction applied to a long-term experiment that emulates multiple Europa flybys. Each Jupiter orbit is one "step" in the blue line of uncorrected measured RadFET data. The near vertical portion of each step represents the high dose encountered during the flyby, and the more horizontal segments represent the low dose accumulated during the remainder of the orbit. Response fade for each orbit results in a slight negative slope to the horizontal (low dose) portion of the orbit, where the fade manifests itself as an apparent reduction in accumulated dose (the decrease in apparent dose between the red squares and yellow diamonds on the blue line). The corrected values, indicated by the purple circles, cumulatively add these observed fade residuals (pre- minus post- encounter value) to obtain a final, more accurate measurement. Similar to the actual dose, the effects of fade accumulate over time, resulting in an increasing deviation between the corrected and measured values over time, as seen in the detailed view in the green inset box, which highlights the largest corrections at the end of the experiment

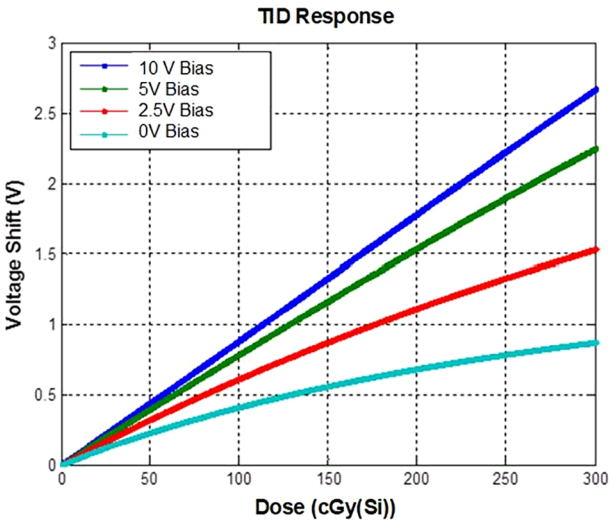

Fig. 15 Dependence of RadFET threshold voltage shift on total ionizing dose for different bias conditions. Note the increasing sensitivity and response linearity with increasing bias

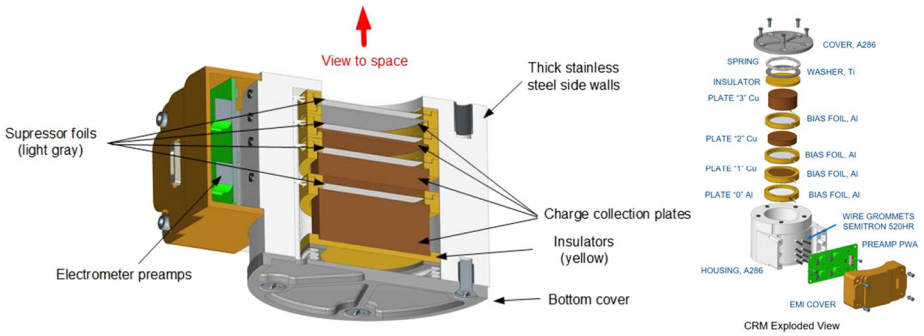

Fig. 16 Left: CRM cross section showing the four charge collection plates separated by suppressor foils. The upper charge collection plate is aluminum and colored gray, while the lower three plates are copper and are colored brown. Right: Expanded view of the CRM

4.4 Charging Current Measurement

The Charge Rate Monitor performs instantaneous net charge measurements of the Jovian electron radiation environment using a stack of four bulk charge collection plates. Incident flux results in a net current across each plate that is a measurement of the charging environment across that plate's effective shielding depth. Due to the CRM's slow response time (>1 s), the CRM output current is a time average measurement rather than a count of discrete particle impact events. The CRM measurement is not selective in terms of particle species. The proton flux provides a net subtraction from the measured electron current, however, the net contribution of protons that reach the shielded CRM plates is less than 1% of the total current in the Jovian environment.

A cross-sectional view of the CRM sensor is shown in Fig. 16. The CRM charge collection plates are stacked below the aperture, with each plate increasing in thickness and providing shielding to the plates below. This arrangement results in each plate collecting a progressively higher energy range while reducing mass and volume. Plates are made from copper, except the uppermost plate (plate 0), where aluminum is used to lower its capture cross section relative to the other plates. All plate diameters are 38.7 mm, with plates 0 through 3 having thicknesses of 0.381 mm, 1.02 mm, 7.24 mm, and 16. 6 mm, respectively. Due to the low charging currents, the plates need to be separated from each other and the housing by highly insulating spacers. We use spacer rings fabricated from Ultem, a polyetherimide. A stainless-steel housing confines the field-of-view of the aperture. The thick side walls lower the fraction of off-axis, lower-energy electrons that reach the thicker lower plates so that the device is most sensitive to higher-energy electrons that can penetrate the plates above. As a simple bulk detector, the CRM has no alignment or bore-sighting requirements.

Between each charge collection plate and above the aperture is a suppressor foil. During CRM operation, a voltage of approximately -30 V is applied to the foils to minimize the impact of secondary electrons generated on one plate moving to another. Periodically, the suppressor voltage, which will be reported in Volts as part of the RadMon data products, is swept to a positive voltage to instead collect the low-energy secondary electrons. The change in response at the different suppressor voltages can be used to characterize the net secondary electron contribution. This operation allows for subsequent correction in the post-processing of the data if needed.

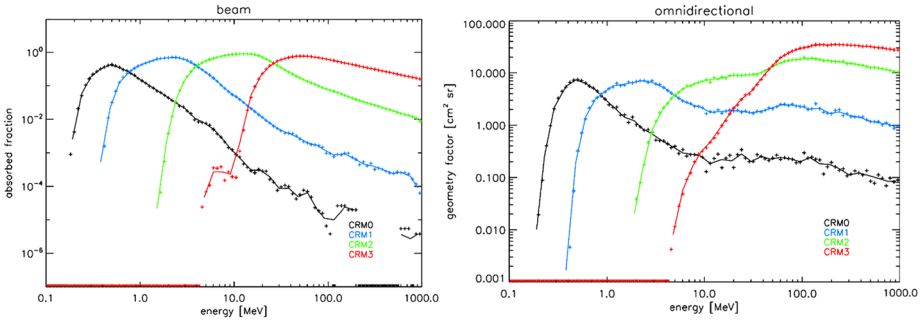

Fig. 17 Simulated CRM response curves with a uniform energy distribution from 0.1 to 1000 MeV. Left: Response to a pencil beam source. The absorbed fraction represents the fraction of primary electrons at a given energy stopped in a given charge plate. Right: Response to isotropic electron distributions (cosine-law source). The relations of the geometry factor to electron intensity and CRM charging current are detailed in Sect. B.2. The simulations include effects from thermal blanketing over the CRM aperture. It can be seen that the different CRM plates respond to increasingly high electron energies

The currents generated by the incident electrons will be of the order of 1 pA for each plate. These low currents are read out by a high-gain transimpedance preamplifier connected to each plate. These preamplifiers are co-located with the charge plate stack in the CRM assembly to minimize noise and leakage. The preamplifier output is subsequently low-pass filtered prior to analog-to-digital conversion. Although the measurement does not integrate over time, the relatively slow time constant of the high-gain, low-current preamplifier circuit results in a slow measurement rate of one sample per second.

The variable thickness of the shielding for each plate allows the CRM to provide four current measurements that can be used to infer a crude four-band electron energy spectrum. GEANT4 simulations (detailed in Sect. C.3) were used to determine plate composition and thickness for the distribution of energy sensitivity bands. Each energy band has a relatively broad range for energy sensitivity and overlaps with the neighboring bands. A calculated energy sensitivity diagram that also accounts for attenuation due to thermal blanketing over the CRM aperture is shown in Fig. 17. The uppermost plate is sensitive to the lowest energies and also registers the highest current. The sensing energy range increases and the current decreases with each plate descending into the stack.

4.5 Ground Calibration

4.5.1 RadFET Characterization

The majority of ground calibration activities focused on the TID measurements. Significant testing with ^{60}Co gamma rays was performed for the initial RadFET selection process as well as detailed characterization. The RadMon dosimeter calibration was carried out using the ^{60}Co irradiator at the Johns Hopkins Applied Physics Laboratory, which is regularly calibrated and checked against National Institute of Standards and Technology (NIST) traceable standards. Although the gamma ray exposure differs from the primary electron-based source of TID at Jupiter, ^{60}Co gamma ray exposure is the standard approach to assessing radiation hardness. The RadFET characterization therefore aligns with the documented radiation tolerance of electronics components and allows them to serve as a good proxy for the spacecraft electronics in general. Electron beam testing using the high-energy electron beam

facility (e.g., at NIST or Brookhaven National Lab) is a possibility if further calibration is needed for either RadFET or CRM measurements (see Sect. 4.5.2).

The dose rate during the characterization tests was controlled by a motion stage internal to the chamber that sets the distance from the source to the RadFETs under test, with the irradiation time determining the total integrated dose. The testing did not include a witness dosimeter, as previous testing has shown levels of unwanted dose enhancement due to backscatter from added nearby materials. For dose response and fade tests, four devices (with serial numbers listed in Figs. 12 and 17) were placed in the radiation chamber at the same time at a distance of 200 mm from the ^{60}Co source and irradiated for 186.52 minutes for a total exposure of 300 krad. Because RadFETs are single-use, these were not identical devices as used in flight but of the same type with matched initial voltage response. Testing for biased devices used a bias voltage of 7.2 V that matches the bias that will be used during the mission. The measured response curves are shown in Fig. 12. As expected, the biased RadFETs display a linear dose-response compared to the non-linearities seen in the unbiased devices. The dose responses of the individual biased devices fall within ∼6% of each other.

The response fade also required ground correction. The fade rate decreases over time as recombination rates in the device's oxide decline. The fade rate also increases with temperature, and consequently, the fade calibration is more complicated than that for temperature.

Several fade experiments have been performed including measuring fade at differing temperatures for periods of up to several months at room temperature. Figure 13 shows the results of apparent dose fade over four days that followed the 300 krad irradiation shown in Fig. 12. There was no additional irradiation during the response fade time. The initial dose was normalized to 1.0. The shown decrease to <1 of the threshold voltage could naively be interpreted as the total dose decreasing, which is impossible, and therefore requires correction based on the measured time dependence of the fade. The fade rate among the biased devices is very well matched across devices. Across multiple experiments, fade over time could be described by a power law fit, with shorter term (under 5 days) and longer-term fade responses requiring different fitting parameters.

Further ground experiments were conducted using a ^{90}Sr electron source and translation stage that varied the distance from the source to the RadFET in a two-week cycle over a 240-day period. The goal of the experiment was to simulate the mission's eccentric Jupiter orbit – with a brief high electron dose for the Europa encounter phase followed by an extended period of relatively low dose. TID was accumulated over a number of cycles with the fade correction applied to each orbit. The correction approach was to use the pre- and post-encounter TID values and separately measure the changing amount of fade occurring between each orbit to cancel the long-term fade that occurs in between each encounter. Results are shown in Fig. 14. This algorithm is estimated to reduce the error due to long-term fade to $<10\%$, which demonstrates the efficacy of the fade correction, with the caveat that each simulated orbit resulted in a higher accumulated TID than is anticipated for the majority of the flight system electronics. Further improvements to the approach are planned to cancel out short-term fade during the encounter itself (∼2 days), which results in an approximately 5% error during an encounter. Modeling of experimental data indicates a sum of two exponential terms will be adequate to model the short-term fade effects. A noted drawback of this technique is that it may miss a small contribution to the total dose that accumulates during the long portion of the orbit further away from Jupiter.

There is also an independent method for estimating fade that was investigated on the Van Allen Probes mission. The technique assumes that the charge monitor plates act as a good proxy for dose rate in an electron-dominated environment, which appears to be the

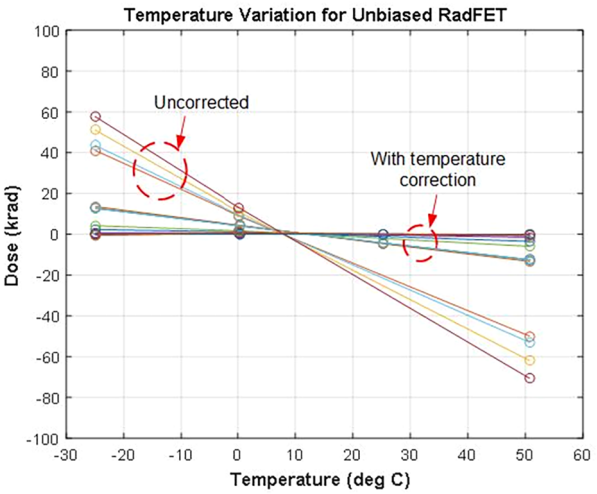

Fig. 18 Example TID temperature response correction for four different RadFET samples after irradiation. Dose in this case refers to deviation from the calibrated received dose of 300 krad, with a value of zero being ideal. The same correction is applied to each of the RadFETs to demonstrate the improved uniformity of the response that can be achieved by correction

case along Europa Clipper's orbit. The exact relation needs to be inferred for Jupiter's hard electron spectrum. Given that the charge plates do not exhibit fade, while the RadFETs do, the charge plate data can be used to derive a correction for the effect. This technique has not been developed sufficiently to provide a detailed uncertainty analysis here, so is considered an area for future work.

As mentioned previously, the selected RadFETs exhibit a strong thermal response in the form of an offset that scales linearly with temperature. As a result, the raw RadFET response data must be corrected for temperature using data from co-located thermistors. Parameters for this correction are provided in Appendix A. Figure 18 shows the measured response and an example correction, all for multiple unbiased RadFETs over a wide temperature range. The temperature dependence can be corrected to significantly reduce the skew in the data. For devices in regions of the spacecraft with lower thermal variations, such as the sensor assembly with a predicted range of roughly 5 °C to 35 °C, the temperature-induced error to the TID increase can be further reduced.

4.5.2 CRM Modeling and Characterization

GEANT4 modeling was the primary approach used for initial development and subsequent refinement of the CRM design. For the model, some aspects of the CRM's construction were simplified, but these changes were limited to combining mechanical components with identical materials, such as merging multiple Ultem insulator ring parts, as well as simplifying structural details beyond the charge collection area such as the spacecraft deck and mounting flanges for preamp electronics. Plate and suppressor foil spacing and thickness dimensions were preserved in the model in order to accurately simulate the energy sensitivity of the plates, which is determined by their dimensions, spacing, and materials.

A key concern during the CRM development was the impact of charge accumulation in the Ultem insulator rings. Modeling indicated that Europa's charge environment, coupled with Ultem's high intrinsic resistance, could result in excessive charging and subsequent discharge events that would damage the preamp electronics. To address this concern, a non-flight version of the CRM hardware, which was structurally identical to the flight unit, was tested in vacuum using a higher activity ^{90}Sr source with a penetrating electron flux approximately five times the worst case of 40 hour near-Europa electron fluence environment. After

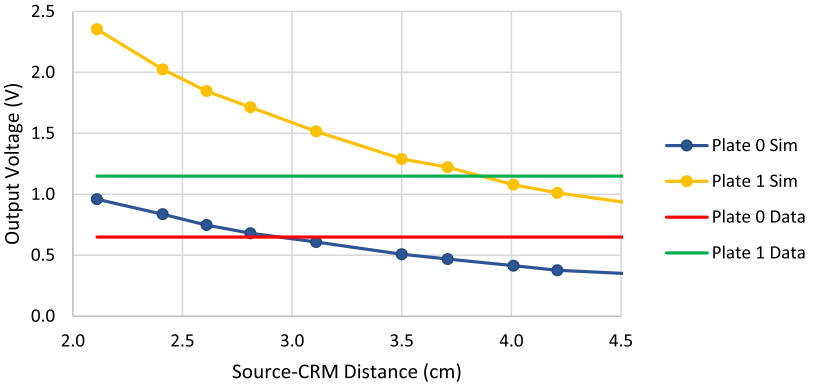

Fig. 19 GEANT4 simulation results for CRM Plate 0 and Plate 1 responses vs. separation between CRM to ^{90}Sr source (lines with points). Solid straight lines represent measured response at a separation of 3.5 cm

a five-day bakeout to eliminate any moisture trapped in the Ultem rings, the experiment was run for a three-week period at 5°C, the lowest predicted CRM operating temperature. While there were discharges observed, the CRM preamp response did not exhibit any change in performance, indicating that the electronics are robust to the level of discharges that could occur during the mission. Overall, the experiment represented an estimated total charging of 13 Europa encounters with dielectric charging currents as high as 3.8 pA.

While the primary purpose of this experiment was to observe the generation, magnitude, and survivability of discharge events within the CRM, it also served as an opportunity to characterize the response of CRM Plates 0 and 1. As part of the characterization, a GEANT4 model of the ^{90}Sr source was developed, using the manufacturer's specifications. This source model was combined with the CRM model to generate predicted CRM response curves that could be compared with experimental results. Figure 19 shows simulated results for a variety of source to CRM separations, with the straight lines showing the experimental values at the 3.5 cm separation used during test. At the experimental distance, the simulated value was -22% of experimental for Plate 0, with a simulated value $+12\%$ of experimental for Plate 1. These results indicate that the CRM model is benchmarked within $\sim 20\%$ uncertainty of the experimentally observed CRM outputs.

Additional CRM calibration for the flight hardware was limited to characterizing leakage currents over temperature during thermal vacuum testing. These leakage currents will be treated as offsets to the measured current values, using the temperature sensor on the CRM preamp as the temperature reference.

4.6 Data Products and Data Archiving

The RadMon Data Extractor Tool will aggregate raw TID sensor telemetry as uncorrected digitized RadFET drain voltage measurements directly from the analog-to-digital converter. Aggregated data will include TID measurements from the various RadFETs distributed across the flight system, i.e., the Sensor Assembly, DTID from the avionics REU telemetry, and the individually hosted sensors within PIMS, Europa-UVS, and the avionics. Temperature telemetry from each corresponding nearby temperature sensor will also be collected in the raw data set of the TID measurements. A response curve and subsequent temperature correction will be applied to arrive at a preliminary TID measurement value in physical units of krad for each sensor.

After release of the initial TID data product, subsequent higher-level data processing will apply the fade corrections. It is anticipated that the fade correction can be fully automated and included in the software tool when the in-flight calibration is completed after several Jupiter orbits. The calibration will be updated periodically using the more sensitive and linearly biased RadFETs as a reference for the more common unbiased, distributed RadFETs. Recalibrating the unbiased RadFETs' responses may be required at higher (>50 krad) TID levels due to the gradual decrease in sensitivity of the unbiased devices relative to the biased devices. By that time in the mission, it will be possible to determine the relative dose rates experienced by each RadFET, which will vary by location due to variations in effective shielding. An ensemble average of the unbiased RadFET response that accounts for these different rates will be compared with the biased RadFET response. Deviations in the unbiased response can then be readily modeled. Updated calibration information will be used to update the RadMon Data Extractor Tool. Details on the current TID calibration equations are given in Appendix A.

The CRM data is more straightforward to process. Digitized voltage outputs from the transimpedance amplifiers described in Sect. 4.4 will be collected from the four Sensor Assembly channels. Conversion to net charging current in physical units of pA is achieved by dividing the voltage by the transimpedance amplifier's feedback resistance. A flux estimate can be obtained using the charge collection disk area of 12.38 cm^2. Values will be corrected for the thermal dependence of the preamplifiers' leakage offsets to yield a fully calibrated data product. Details on CRM calibration and calculations are given in Appendix B. Finally, the instantaneous CRM and time-integrated TID measurements may be cross-calibrated to further refine the TID measurements.

4.7 Operations Plan During Cruise and Tour

Operationally, the RadMon is quite simple. The sensor assembly will be powered on shortly after launch so that the biased RadFETs can begin to accumulate TID. The sensor assembly will then transition to a regular measurement collection of TID and charge measurements at a rate of once per second. TID and charge data are included as part of the sensor assembly housekeeping telemetry, i.e., there are no dedicated radiation data packets. TID data from the DTIDs and hosted TID RadFETs are similarly embedded in the REU or host electronics' 1-Hz housekeeping telemetry.

Absent any anomalies for host electronics or the spacecraft, this nominal measurement cadence would continue regardless of whether the mission is in the cruise or Jupiter tour phase. During the cruise phase, TID will accumulate relatively slowly and charge measurements will be at a low level, given that the CRM is tuned for high fluxes in the Jovian environment. Flight software will decimate the radiation data prior to downlink given that its variation is expected to be very slow. During Europa encounters, CRM data is unlikely to be heavily decimated. However, some decimation of TID data will still occur because the integrating detectors will have a response that will be relatively slowly varying. In other words, the charge rate monitor provides a more instantaneous reading of the ambient charging environment. The charging environment impacts the TID measurement as well, albeit with a relatively smaller net change due to the integrated nature of the TID measurement. To decrease decimation, we have therefore prioritized CRM data return rate during flybys.

5 Opportunistic Radiation Data from Other Europa Clipper Science Instruments

While the RadMon is the main source of radiation data, opportunistic data from science instruments onboard the Europa Clipper could supplement the primary dataset. In this section, we provide a brief overview of these possible radiation measurements. Especially, sensitivity to different energy thresholds can be extremely useful to construct or constrain the shape of the energy spectrum. As noted earlier, the information about energetic electrons will be mainly obtained from this collective effort among the different science instruments along with the RadMon. The limits on instrument measurements with respect to radiation noise and potential optimization of instrument settings to increase science return under these conditions may also be discussed in the individual instrument papers in this collection.

5.1 Europa Imaging System (EIS)

The EIS (see separate publication in this collection) will image Europa's surface features in great detail using a wide-angle camera (WAC) and a narrow-angle camera (NAC), each of which has silicon detectors, specifically 4k $\times$ 2k CMOS detectors (Janesick et al. 2014). While EIS uses passive shielding to mitigate the radiation damage to its electronics and detectors, sufficiently high energy particles will be able to penetrate the shielding and generate charge in random pixels within the camera detectors. Information of the radiation environment may be extracted from the resulting "noisy" images. For example, the noise data acquired of black space or Europa's night side provide information on the high-energy flux in the Jupiter system, as was achieved with the Galileo Solid State Imager (Klaasen et al. 2003). The best EIS images for measuring radiation hits will be dark frames acquired for calibration and long-exposure images taken to search for plumes. The EIS will take images at many Jovian longitudes and ranges from Jupiter and Europa, thus contributing to a record of how the flux varies with these parameters as well as its variation over longer timescales. As part of the search for small plumes, EIS will also image Europa's night side just beyond the terminator at a low altitude, which will provide radiation data very close to the surface of Europa. We expect that the EIS data will be useful to study the temporal variability of the Jovian radiation environment. Because each energetic particle hit generates charges over multiple pixels and causes secondary radiation effects, evaluation of the energetics of Jovian radiation environment from such data can be complicated. A preliminary shielding analysis indicates that EIS would be primarily susceptible to >10 MeV electrons. EIS images will also reveal morphologic or color/photometry variations of Europa's surface that may be explained by energetic particle interactions (Hand and Carlson 2015).

5.2 Europa-Ultraviolet Spectrograph (Europa-UVS)

The Europa-UVS (see separate publication in this collection) detects ultraviolet light with a telescope and separates its wavelengths with an optical grating, with the ultimate goal of identifying the composition of Europa's surface. The measurement is achieved by using an MCP detector. Europa-UVS uses a high-Z (where Z is the atomic number) alloy shielding material (TaW) to mitigate the radiation damage to the electronics and detectors. However, penetrating high energy particles can generate noise signals within the detector. The detector of the Juno-UVS instrument is susceptible to energetic electrons, and the data has been used as a proxy for >6 MeV electrons (Sect. 2.1.1). The same approach can be used for the Europa-UVS instrument to extract the radiation environment information. A preliminary

radiation transport simulation indicates that the Europa-UVS is sensitive to >10–15 MeV electrons, thereby providing another valuable high-energy electron "channel". The Europa-UVS instrument includes one of the RadMon's hosted RadFET dosimeters.

5.3 Mapping Imaging Spectrometer for Europa (MISE)

The MISE will detect and analyze infrared light reflected from Europa with the main goal of mapping Europa's surface composition (Blaney et al., this collection). A Mercury-Cadmium-Telluride (MCT) infrared detector is used for the measurements. MISE uses a high-Z shielding material (Ta) to mitigate the radiation damage to the electronics and detectors. The MISE MCT detector is also susceptible to radiation, and the energetic particles will generate the background noises in the measured images. As observed with Galileo NIMS, γ-rays created through electron bremsstrahlung will also contribute heavily to radiation noise detected by the MISE, especially at longer wavelengths (>3 μm) where the solar reflectance signal decreases significantly (Carlson and Hand 2015). Similar to the EIS, the radiation data from the MISE will be primarily taken from dark frame information, which in the case of the MISE are "stacks" consisting of images taken at multiple wavelengths. The MISE radiation measurement information will also be used with other radiation data to understand how Europa Clipper's radiation environment during a given encounter period can be extrapolated to the post-encounter period. However, if there is a significant disconnect between the MISE dark frame statistics and the measured radiation environment, it may indicate that an update to the dark stack processing is required. This update would be a tactical use of the RadMon and other radiation data to improve the performance of another Europa Clipper instrument. It is estimated through radiation transport simulation with beam tests that, because of the very thick shielding used, the MISE can provide information on electron fluxes >50 MeV. This instrument is therefore a valuable data source for extremely energetic electrons, which are not readily available from other means on the spacecraft or from measurements on previous missions.

5.4 MAss Spectrometer for Planetary EXploration (MASPEX)

The MASPEX is designed to detect, identify, and quantify the abundance of neutral gases produced by radiolysis, sublimation, or interior outgassing from the surface of Europa (see Waite et al., this collection). The MASPEX MCP detects the ionized neutral gas molecules based on their temporal dispersion using a time-of-flight mass analyzer. As described in Sect. 5.2, the MCP detector is also sensitive to penetrating radiation and secondary photons, thus creating a radiation induced noise background. During a Europa flyby, the MASPEX can take radiation background measurements when not registering ion signals during normal operations (or interleaved with normal operational measurements). These measurements are noise measurements or particle flux measurements, which can be directly correlated and compared to outputs from the RadMon's CRM. The results from the CRM can be used in a Monte Carlo particle transport simulation with instrument geometry of the MASPEX to provide an expected background radiation noise count value. A direct comparison of this simulation with inflight measurements from the MASPEX during the Europa flybys can be used to determine the accuracy of the GIRE and JOSE models of the near-Jupiter proton and electron environments derived from Galileo and other Jupiter mission data. A preliminary analysis indicates that the MASPEX can infer the electron flux for energies >3 MeV and could serve as a secondary source of input in the overall modeling process.

5.5 Plasma Instrument for Magnetic Sounding (PIMS)

Jupiter's magnetic field carries plasma from the volcanic moon Io, Jupiter's ionosphere, and Europa itself. The plasma flow near Europa generates a magnetic field that must be accounted for in the induction experiment to characterize Europa's ice shell and ocean. The PIMS will measure the density, temperature, and flow of plasma near Europa (Westlake et al., this collection) to correct the magnetic induction signal for plasma contributions, which is important to precisely determine Europa's ice shell thickness, ocean depth, and conductivity. The PIMS consists of two sensors, one at the top of the spacecraft and one at the bottom of the spacecraft, each containing two Faraday cups. These cups are large aperture plasma instruments that measure the current of particles that hit the segmented metal collector. The PIMS utilizes high voltages applied to an array of grids in the instrument aperture with a characteristic 320 Hz sine wave to produce an AC-coupled measurement. This measurement locks onto only the particles generating a signal modulated at the same frequency as the applied sine wave and effectively removes the background signal caused by UV, dust impacts, and energetic particles. With the voltages applied to the grids, the PIMS will be able to measure ions up to 6.6 keV and electrons up to 2.2 keV. The PIMS also measures an integral or DC current at each voltage step, and this measurement sums the currents from each of the three segmented collectors within the instrument and yields a total current registered by the instrument. The total current includes contributions from UV photons, dust impacts, and energetic particles, and thus does not provide an energetic particle measurement of high quality (that is, it does not provide any specific energy "channel"). However, it can provide a diagnostic of the presence of energetic particles during any given measurement, thus providing information on the high-energy electron environment.

5.6 SUrface Dust Analyser (SUDA)

The SUDA detects the ejecta or dust from the Europa surface resulting from micrometeorite impacts and analyzes them to identify the physical properties of dust and ice grains and their chemical composition through mass spectra, revealing Europa's surface composition including potential organic molecules (Kempf et al., this collection). The SUDA's target and detector are directly exposed to open space and contain a rejection grid to reduce incoming thermal plasma that can interfere with the normal operation of the instrument. However, if incoming electrons and ions are sufficiently energetic, they will be able to pass through this rejection grid to reach the interior and could be detected as random current spikes as they impact the target and/or detector surfaces. The SUDA's rejection grid is nominally set to $+/-$ 3.2 keV and its reflection grid is set to $-/+$ 2.8 kV (positive or negative bias depending on whether it is in anion or cation-sensing mode, respectively). This means that radiation at energies $>|\sim 3$ keV/q| will be able to penetrate into the instrument, where q is the ion charge state ($+1$, $+2$, and $+3$ are common heavy-ion charge states). Data generated by such high-energy particles will be automatically recorded by the SUDA and stored in its memory for the duration of the mission. As in the case for the PIMS, the SUDA's high energy particle data would be qualitative in that only the total current will be measured; hence it provides a diagnostic measure of the state of the general radiation environment. The data from the RadMon and other instruments can be used to further constrain the radiation data from the SUDA. It would also be possible through laboratory tests or detailed numerical simulations that the magnitude of the current during the recorded impact could be used to extract the energy of the incoming particle. The SUDA continuously monitors the current, which can be converted into a time-dependent measure of the incoming radiation.

6 Potential Science Enabled by the Europa Clipper Radiation Measurements

As described in Sects. 4 and 5, the Europa Clipper spacecraft will be able to measure the high energy ($>\sim$1 MeV) electron environment as a function of time and trajectory location with a one second cadence (in the case of the RadMon TID and charging rate measurement). This rich set of high-energy electron data could be applicable to investigate various possible scientific topics outlined in Sect. 2.3. This section summarizes potential radiation science that can be achieved with these measurements in terms of space physics and surface science.

6.1 Space Physics: Particle Acceleration and Variability of Trapped Electrons

In the Jovian magnetosphere, quasi-relativistic to relativistic particles are detected at a large range of radial distances. One of the fundamental questions that space physics seeks to answer is how very energetic charged particles are created. Cosmic rays can be the source of some energetic charged particles, while others are likely accelerated from the plasma energy range. Jupiter is an especially good laboratory for studying particle acceleration because its conditions bridge the exploration of the Earth's radiation belts and remote observation of objects such as supernova remnants or brown dwarfs (Mauk 2012). As for the acceleration mechanisms, two main candidates at Jupiter include: any process that drives charged particles across L shells such as injections and radial diffusion, and wave-particle interactions. These two acceleration processes can be distinguished by tracking a sharp cutoff of the electron spectrum throughout the magnetosphere (Kollmann et al. 2018), where the particle spectrum based only on the adiabatic acceleration is shown to have a sharp cutoff at high energies that coincides with the resonant energy at which the magnetic and electric drifts cancel each other (Roussos et al. 2018; Hao et al. 2020). However, the available data to construct the wide energy spectrum are insufficient to reliably retrieve spectral cutoffs near Europa's orbit based on the data from previous missions, especially for electrons. This cutoff is expected to be around 20 MeV at Europa's orbit and therefore will be directly constrained by the RadMon data. These spectra would allow us to distinguish adiabatic from local wave interaction processes. Also, if the spectra indeed show this cutoff, it will provide further support that the hemispherical asymmetry on Europa's surface is a result of electron weathering (Patterson et al. 2012): While one hemisphere is bombarded in a lens-shaped pattern with significant intensities of $<$20 MeV electrons, $>$25 MeV electrons only reach the opposite hemisphere and have insignificant intensities due to the described cutoff in the spectrum.

Variations of the trapped electron environment can be dynamic. Occasionally the intensities of $>$10 MeV electrons rise by several orders of magnitude for reasons that we can currently only speculate about. The Galileo EPD data showed that there can be a burst of electron flux enhancement on timescales of a few hours to a few days. An example is a C22 "storm" (see Sect. 2.3). Measuring the electron population above one MeV during the Europa Clipper mission may provide a clue to understand the physical mechanism(s) responsible for the occurrence of those bursts within the trapped environment. Measurements of the high-energy electron environment covering the wide L ranges over the planned Europa Clipper mission lifetime could also provide an opportunity to compare long-term variation of the trapped environment at different regions within the Jovian magnetosphere – how the high energy electron environments are different between the Europa Clipper era and the Pioneer, Voyager, Galileo, and Juno eras. It is also possible that the RadMon measurements of the asymmetric electron radiation around Europa could benefit planning of instrument operations for each flyby.

The solar wind influences the planetary magnetosphere. In the case of the terrestrial magnetosphere, the solar wind can cause drift paths being close to Earth. However, Jupiter is "rotationally dominated," and the Jovian radiation belts are somewhat protected from solar wind disturbances. This may be one of the factors that create radiation belts at Jupiter that are so intense. Unlike at Earth, the high-energy electron energy spectrum falls off very slow with increasing energy. However, while it has been previously postulated that the solar wind does not strongly influence the radiation belt in the region $L<10$ at Jupiter, recent studies indicate that there may be links between the solar wind and this region that needs to be explored further (e.g., Murakami et al. 2016). If the timing is fortuitous, the ESA JUICE spacecraft will still be in the solar wind and will monitor disturbancesin this region while the Europa Clipper is already in Jupiter orbit observing the effects. Furthermore, any two-point simultaneous measurements by the Europa Clipper and JUICE spacecraft could provide a synergistic opportunity to understand the overall state of the magnetosphere.

As discussed in Sect. 2.3, the environment near Europa is not uniform and varies dynamically because of the local electromagnetic environment perturbations. Knowing the electron environment near Europa would allow us to further our understanding of the precipitating pattern to the surface. For example, high cadence measurements of the high-energy electron environment in the vicinity of Europa from multiple flybys could be very useful to understand the asymmetric nature of the electron bombardment pattern between the leading and the trailing hemispheres as a function of electron energy.

6.2 Surface Science

Due to its presence deep within the Jovian radiation belts, Europa's surface is strongly altered by the bombardment of magnetospheric charged particles (Johnson et al. 2004; Carlson et al. 2009; Paranicas et al. 2009). Radiation can modify the crystal structure and/or change the chemistry of surface materials on a variety of timescales (Hand and Carlson 2015; Poston et al. 2017). This includes thermal magnetospheric plasma which nearly corotates with Jupiter's magnetic field, and thus overtakes Europa in its orbit and preferentially bombards its trailing hemisphere (Saur et al. 1998; Kivelson et al. 2004; Harris et al. 2021). In addition to these low-energy plasma populations, Europa is also bombarded by energetic charged particles (primarily electrons, protons, and charged states of oxygen and sulfur) in the keV to MeV energy range (Paranicas et al. 2001, 2002; Mauk et al. 2004; Paranicas et al. 2007; Jun et al. 2019b). These energetic charged particles bombard Europa's surface in a highly non-uniform fashion, and attempts have been made to predict their weathering pattern (Pospieszalska and Johnson 1989; Paranicas et al. 2001; Addison et al. 2021). Energetic electrons represent the largest contribution to the surface radiation (Paranicas et al. 2007) and are expected to bombard the surface in a lens-like pattern centered on the low-latitude trailing hemisphere and leading hemispheres (Paranicas et al. 2001; Truscott et al. 2011; Patterson et al. 2012; Nordheim et al. 2018). This expected bombardment pattern appears to roughly correlate with the presence of an unknown hydrated species (possibly H_2SO_4) on the trailing hemisphere (Paranicas et al. 2001; Carlson et al. 2005; Grundy et al. 2007; Brown and Hand 2013; Fischer et al. 2015, 2016; Ligier et al. 2016), meaning that electrons may add energy that allows the sulfur originated from Io to form hydrated sulfuric acid. The leading hemisphere shows a radiolytic H_2O_2 (Carlson et al. 1999a; Trumbo et al. 2019). Laboratory measurements show that peroxide is formed via radiation processing of pure ice at the level of $<1\%$ by number, relative to water, and other compounds may mediate its formation (Moore and Hudson 2000; Hand and Carlson 2011). On Europa, peroxide serves as a strong indicator of the radiolytic processing of ice. At this time, our understanding of the exact radiation fingerprint on the surface has been based purely on the modeling of

particle trajectories with many simplifying assumptions. Europa Clipper data could be used as an input to trace particle trajectory simulations in a complex perturbed electromagnetic environment near Europa and constrain the surface weathering pattern by correlating these simulations with measurements from other instruments onboard Europa Clipper, such as the EIS and MISE.

Energetic ions are thought to be responsible for the production of amorphous ice observed on Europa's surface (Hansen and McCord 2004; Ligier et al. 2016; Mitchell et al. 2017; Paranicas et al. 2018a; Berdis et al. 2020), as well as sputtering of gases that contribute to Europa's atmosphere, and implantation of sulfur ions (Cassidy et al. 2013; Breer et al. 2019; Addison et al. 2021). Europa's surface geology due to radiation bombardment is therefore an important context for observations that will be made by multiple Europa Clipper instruments, including estimations of surface properties such as grain size (Clark et al. 1983; Cassidy et al. 2013) and composition from the MISE instrument (Blaney et al., this collection). Furthermore, Europa's tenuous exosphere is likely due to surface radiolysis and sputtering (Plainaki et al. 2010; Cassidy et al. 2013; Plainaki et al. 2018; Davis et al. 2021), and will therefore be key to understanding the measurements of Europa's exosphere by the MASPEX instrument (see separate publication in this collection). However, many questions remain unanswered, particularly regarding the variability of charged particle fluxes across Europa's surface and the response of charged particles to the locally perturbed electromagnetic environment near the moon. The measurements from the Europa Clipper combined with future laboratory work, guided by radiation and spectral observations, could advance our understanding of the effects of radiation on Europa's surface.

6.3 Radiation Science Relevant to the Europa Clipper Thematic Working Groups

Although radiation science itself does not have direct implications for fulfilling the mission's Level-1 science objectives, the radiation data collected from the mission can indirectly help achieve some of those Level-1 science objectives by supporting all the radiation-affected instruments on expected radiation levels for each flyby so that instrument states could be accurately commanded for these flybys to maximize the science return, e.g., to detect the ocean-ice interface with REASON, magnetically probe the ocean with the Europa Clipper Magnetometer and PIMS, and gravitationally probe the interior with radio science. Specifically, the radiation data and its interpretation are closely related to the topics that are addressed by Europa Clipper's Composition and Interior Working Groups and the Habitability Advisory Board. Understanding the radiation environment on Europa's surface is critical to constraining the composition on the surface of Europa (from radiolysis) and the exosphere environment (via sputtering). The high energy electron data can help improve our understanding on the relative role of energetic electrons on induction, compared to the thermal plasma. These all could provide possible clues on the questions surrounding the habitability, origin, and evolution of the surface. For example, if a compound is found on Europa's surface, whether it is a radiation product or a material extruded from the ocean. Europa shows a leading-trailing hemisphere dichotomy with the trailing side having greater impact from magnetospheric radiation. The signatures on the trailing side have been interpreted as both salts (e.g., from Europa's ocean) (McCord et al. 1998, 1999) and sulfuric acid, a radiation product (Carlson et al. 1999b, 2002, 2005). Hydrogen peroxide, H_2O_2, has also been identified. The mixture of hydrogen peroxide and sulfuric acid is very destructive to organic molecules but the amounts of hydrogen peroxide in the surface ice may be too small for substantial destruction to occur; hence more work is needed to better understand the role of radiation in producing H_2O_2. Furthermore, the radiation energy flow into the surface may be

an agent for producing materials favorable to life (Hand et al. 2009). While radiation is often considered an agent that lowers the habitability of a surface and degrades biosignatures on it, it also drives the production of compounds that can act as an energy source for life: The irradiation of carbon-rich ice leads to the formation of HCHO, which can act as the sole carbon source for some bacteria. If material produced on the surface is or has been transported to the subsurface ocean, it may have played a role in supporting life (Chyba 2000). See the habitability and composition papers (Vance et al. and Becker et al., this collection, respectively) for more detail.

7 Summary and Conclusion

The Europa Clipper mission is NASA's flagship mission to Jupiter to investigate the habitability of this icy moon. The spacecraft is scheduled to launch in October 2024 and will enter into the Jovian system in 2030, venturing into the harsh radiation environment. The mission will perform multiple (∼50) flybys of Europa, and the radiation environment will be continuously monitored during the mission. Measurements of the radiation environment will primarily be done using a dedicated radiation monitor (RadMon) at a 1 Hz cadence. Total ionizing doses (TID) will be measured by a RadFET stack in a stand-alone RadMon sensor assembly as well as by distributed and hosted RadFET devices located across the spacecraft. These TID measurements will be mostly providing information about electron environment as the electrons are the dominating TID contributor at all shielding levels (see Fig. 2). The electron currents will be directly measured by the charge rate monitor (CRM) located within the RadMon sensor assembly. CRM will be able to measure the >1 MeV, >10 MeV, and >20 MeV electrons.

In addition to RadMon, it will be possible to obtain information on the radiation environment from several of the science instruments using the opportunistic radiation background data that they will collect. Those science instruments include the Europa Imaging System (EIS), the Europa-Ultraviolet Spectrograph (Europa-UVS), the Mapping Imaging Spectrometer for Europa (MISE), the MAss Spectrometer for Planetary EXploration (MASPEX), the Plasma Instrument for Magnetic Sounding (PIMS), and the SUrface Dust Analyzer (SUDA). Comprehensive radiation transport analyses are planned to understand the sensitivity of each instrument to incoming radiation in terms of energy and flux. Depending on the effective shielding level for each instrument, we expect to be able to measure >3 MeV (MASPEX), >10 MeV (Europa-UVS), and >50 MeV electrons (MISE). The RadMon data and the data from these instruments will be used to understand and correlate the responses of other instruments (PIMS, SUDA, and EIS) to radiation, thus expanding the overall radiation measurement capability for the mission while also aiding the instruments in planning optimal settings to minimize radiation noise during each flyby.

Jupiter's magnetosphere is a scientifically fascinating target, with many science questions to be answered. RadMon is nominally an engineering resource supporting radiation hazard assessment, mitigation, and science optimization for spacecraft and instrument systems. As the only radiation detector suite onboard, however, it also provides unique science data on the Jovian magnetosphere and its interactions with Europa. For example, the high-energy electron measurements from the Europa Clipper covering $9-50$ Rj in the equatorial region over the mission lifetime will be a valuable resource to investigate short- and long-term dynamics of the Jovian radiation environment. It could also help us understand the physical mechanisms responsible for the energization of trapped electrons. Furthermore, the Europa Clipper will measure the high-energy electron environment near Europa, where the motion

of charged particles is perturbed by the local electromagnetic environment. The data could also help understand the radiation environment on Europa's surface, which is important for understanding the composition, origin, and evolution of the surface. During the interplanetary cruise through the heliosphere to Jupiter, RadMon can also provide essential engineering data on spacecraft operations and important science data on the interplanetary radiation environment and its response to solar activity.

Appendix A: Housekeeping Calibration Values

The RadMon components show a temperature dependence, which is why we need to track temperatures. Various sensors across Europa Clipper provide temperature measurements as integer "data number" (DN) values. For the Sensor Assembly sensors (on the RadFET stack, the CRM, and the event board), their conversion to °C works as

$$T[^{\circ}C] = -1\text{E}2.12 + 1\text{E} - 1.79 * DN$$

The CRM suppressor voltage is calibrated as

$$\textit{Suppressor Output}\ [\text{V}] = -6.164\text{E} + 01 + 9.644\text{E} - 03 * DN$$

Appendix B: RadFET Calibration Values

B.1 From Raw Measurements to Total Ionizing Dose

The RadFETs originally provide their dose-sensitive threshold as DN values. The conversion to the RadFET voltage U_{RadFET} (usually in Volts V) works for the biased FM RadFETs in the Sensor Assembly as

$$U_{RadFET} = 7\text{V} * DN/16383$$

And for the unbiased as

$$U_{RadFET} = 3\text{V} * DN/16383$$

The voltage converts to dose as follows. For RadFETs biased with 7.2 V:

$$Dose[\text{krad}] = 100 * U$$

For unbiased RadFETs,

$$\text{Dose[krad]} = 114.66\ U^5 - 160.99\ U^4 + 147.55\ U^3 + 25.262\ U^2 + 158.2\ U + 0.26169$$

With the voltage change U from their reference state:

$$U = U_{RadFET} - U_0$$

The reference voltage U_0 for the RadFETs is temperature dependent as shown in Fig. 20. The temperature dependence is described though a polynomial function following:

$$U_0 = A_{[0]} + A_{[1]} * T + A_{[2]} * T^{\hat{}2}$$

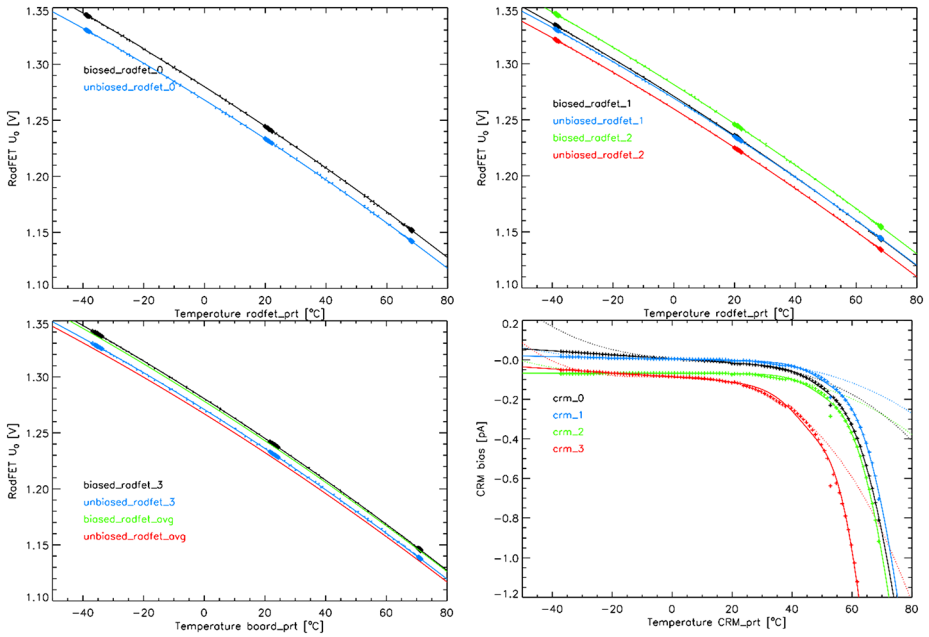

Fig. 20 Upper row: Temperature dependence of reference voltage U_0 of the RadFETs within the TID stack. Lower left: Temperature dependence of reference voltage U_0 of RadFETs of the Sensor Assembly board over the temperature of the board. We also show the average behavior of RadFETs over their respective temperature. Large symbols show measurements taken at times where temperature was stable for several hours, small symbols when it was changing. Solid curves show the polynomial fits with parameters as tabulated. Lower right: Change of the CRM bias current I_{bias}. Plus symbols show binned data. Dashed curves show the simple polynomial fit that is best for 0-40C. Solid curve shows the fit with the more complicated function. All results shown here are from the thermal-vacuum test in 2022/May/2-7

The parameters in Table 2 are for temperatures T being measured in °C. The temperature sensor most representative for RadFETs 0-2 in the TID stack (both biased and unbiased) is RADFET_PRT_MUX. RadFETs 0 are the lowest shielded in the TID stack, with RadFETs 1 in the middle and RadFETs 2 most heavily shielded. For RadFETs 3 on the board of the Sensor Assembly (both biased and unbiased) it is BOARD_PRT_MUX. RadFETs that are at other locations (within an instrument or a vault, see Fig. 7) have not been explicitly calibrated but will behave similarly to the ones of the Sensor Assembly. We therefore also provide average parameters in the table that can be used for these devices together with a temperature measurement from the temperature sensor closest to them.

B.2 From the Dose to Electron Intensity

For the scientific analysis, it will be possible to convert the RadMon RadFET measurements into differential intensity j (electrons per interval in time, energy, area, and solid angle). A dose R is defined as the total deposited energy per mass. For the RadFETs, we can use the following expression:

$$R = \frac{\int_0^\infty \epsilon E_d j 4\pi A dE}{\rho A h} \approx \frac{\int_0^\infty \epsilon \frac{dE}{dx} j 4\pi dE}{\rho}$$

Table 2 Numerical Vaules for Parameters $A_{[0]}$, $A_{[1]}$, and $A_{[2]}$ used in Equation for U_0

RadFET	$A_{[0]}$	$A_{[1]}$	$A_{[2]}$
biased_radfet_0	1E0.1072	−1E-2.763	−1E-5.644
unbiased_radfet_0	1E0.1031	−1E-2.773	−1E-5.619
biased_radfet_1	1E0.1041	−1E-2.766	−1E-5.649
unbiased_radfet_1	1E0.1036	−1E-2.777	−1E-5.618
biased_radfet_2	1E0.1077	−1E-2.767	−1E-5.649
unbiased_radfet_2	1E0.1003	−1E-2.774	−1E-5.622
biased_radfet_3	1E0.1074	−1E-2.762	−1E-5.626
unbiased_radfet_3	1E0.1041	−1E-2.771	−1E-5.600
biased_radfet_avg	1E0.1066	−1E-2.765	−1E-5.642
unbiased_radfet_avg	1E0.1028	−1E-2.774	−1E-5.615

where ε is the efficiency of electrons reaching the respective RadFET and can be taken from Fig. 11b. E_d is the energy deposited (here mostly by electrons as only a few ions make it to the RadFETs) of energy E in the considered object (in this case the RadFET oxide) with area A and thickness h. dE/dx is the differential energy loss of particles with energy E. The approximation shown here is good for thin objects (such as the oxide layer). ρ is the material density (in this case for SiO_2).

Determining the parameter j will be an ongoing effort while in orbit around Jupiter. The process is anticipated to be a forward model (e.g., Kollmann et al. 2021) where j is assumed, the expected R is calculated, and then j is changed until the expectation matches the measurement, followed by analysis to determine the uniqueness of j.

Appendix C: CRM Calibration Values

C.1 From Raw Measurements to the Charging Current

For the CRM, the output voltage U_{mux} can be retrieved from the measured data number with

$$U_{mux} = DN/16383$$

The voltage U_{mux} is related to the charging current I_{CRM} (in ampere A if units below used as-is) as

$$U_{mux} = U_{preamp} * attenuation + offset$$
$$U_{preamp} = -(I_{CRM} + I_{bias}) R_{feedback}$$
$$R_{feedback} = 101.1\ \mathrm{G\Omega}$$
$$attenuation = 2/5$$
$$offset = 0.1\ \mathrm{V}$$

The bias current I_{bias} is temperature dependent, see Fig. 20. The temperature sensor most representative for the CRM is called CRM_PRT_MUX. For the temperature range 0-40 °C,

Table 3 Numerical Values for Parameters $A_{[0]}$, $A_{[1]}$, $A_{[2]}$, and $A_{[3]}$ used in the First I_{bias} Equation

CRM	$A_{[0]}$	$A_{[1]}$	$A_{[2]}$	$A_{[3]}$
crm_0	+1E-2.15	−1E-2.89	+1E-4.52	−1E-6.00
crm_1	+1E-2.34	−1E-4.07	−1E-5.56	−1E-6.30
crm_2	−1E-1.17	+1E-3.82	−1E-5.63	−1E-6.21
crm_3	−1E-1.06	−1E-3.87	−1E-4.57	−1E-5.72

Table 4 Numerical Values for Parameters $A_{[-2]}$, $A_{[-1]}$, $A_{[0]}$, $A_{[1]}$, $A_{[2]}$, $A_{[3]}$, and $A_{[4]}$ used in the Second I_{bias} Equation

CRM	$A_{[-2]}$	$A_{[-1]}$	$A_{[0]}$	$A_{[1]}$	$A_{[2]}$	$A_{[3]}$	$A_{[4]}$
crm_0	+1E-2.29	−1E-2.99	1E1.70	1E0.51	−1E-0.68	1E-1.92	−1E-2.6
crm_1	+1E-2.45	−1E-3.49	1E1.72	1E0.54	−1E-0.61	1E-1.83	−1E-2.5
crm_2	−1E-1.16	−1E-4.54	1E1.71	1E0.55	−1E-0.58	1E-1.87	−1E-2.5
crm_3	−1E-1.06	−1E-2.99	1E1.69	1E0.63	−1E-0.25	1E-1.55	−1E-2.2

which covers the range expected for the mission, we can fit I_{bias} with a simple polynomial function:

$$I_{bias} = A_{[0]} + A_{[1]} * T + A_{[2]} * T^{\hat{}2} + A_{[3]} * T^{\hat{}3}$$

The parameters in Tables 3 and 4 are for T being measured in °C and yield I_{bias} in A.

To describe the full temperature range, a more complicated function is needed:

$$I_{bias} = (A_{[-2]} + A_{[-1]}x) + 1/[1 + exp\{(-x + (A_{[0]}))/A_{[1]}\}] \times [(A_{[2]}) + (A_{[3]})(x - (A_{[0]}))^{\hat{}1} + (A_{[4]})(x - (A_{[0]}))^{\hat{}2}]$$

C.2 From the Charging Current to Electron Intensity

The charging current I_{bias} relates to the ambient electron differential intensity (electrons per intervals in energy, solid angle, area and time) spectrum $j(E)$. We assume the intensity to only depend on energy E but not direction or pitch angle, which is reasonable at Jupiter where equatorial pitch angle distributions only vary by a factor of a few (e.g. Nénon et al. 2022).

$$I_{bias} = elementary\ charge * electron\ count\ rate$$

$$electron\ count\ rate = 4\pi \int_0^\infty dE\ G(E)\ j\ (E)$$

here the energy-dependent geometry factor $G(E)$ is provided in Fig. 17 through equations detailed below.

C.3 Geometry Factor Derivation

Here we describe how the energy-dependent geometry factor $G(E)$ can be calculated from our GEANT-4 modeling described in Sect. 4.5.2. The GEANT model emits electrons from a

half sphere into its interior, which implies that the spacecraft perfectly shields electrons from one side. We define the source as an isotropic emitter, meaning that the number of particles dN_i emitted per visible area (as well as per solid angle, energy, and time) is constant for all directions and equal to j. This visible area shrinks when viewed from the side: If Θ is the angle from the normal of a source element with area dA, then the visible area of that element is $dA\ cos\Theta$.

$$dN_i = j\ dA\ \cos\Theta\ d\Omega\ dE\ dT$$

where dT is an arbitrary but small time interval that will cancel out later, $d\Omega = sin\Theta\ d\Theta\ d\phi$ is the solid angle, ϕ is the longitude around the normal, and dA an element on the source area (generally different from an area that could be defined for particle detection).

Integration over inward emission into the half sphere (meaning that Θ only runs until $\pi/2$) yields

$$N_I = A\ \mathrm{j}\ \Delta\mathrm{E}\ \Delta\mathrm{T} \int_0^{\pi/2} d\Theta \cos\Theta \sin\Theta \int_0^{2\pi} d\phi$$

$$j = \frac{N_I}{A\pi\ \Delta\mathrm{E}\ \Delta\mathrm{T}}$$

where A is the area of the source. (In our case $A = 2\ \pi\ r^2$ for a half sphere with radius r.)

Now we define the omnidirectional geometry factor G through the standard convention

$$j = \frac{N_C}{G\ \Delta\mathrm{E}\ \Delta\mathrm{T}}$$

where N_C is the number of detected particles. GEANT determines these through the net charge (accounting for primary and secondary electrons) deposited in the CRM volumes. Combining the two equations for j yields the equation we used for the geometry factor

$$G = \frac{N_C}{N_I} A\pi = \frac{N_C \pi}{F}$$

where we used the definition of the fluence $F = N_I/A$.

For reference, we also provide equations that can be used to normalize differently set up simulations. Direction dependence of particle emission from a surface element dA can be described as

$$dN_i = j\ dA\ \tilde{A}\ d\Omega\ dE\ dT$$

The total number of emitted particles can be calculated as

$$N_I = A\ \mathrm{j}\ \Delta\mathrm{E}\ \Delta\mathrm{T} \int_0^{\tilde{B}} d\Theta\ \tilde{A} \sin\Theta \int_0^{2\pi} d\phi$$

Instead of the isotropic emission with $\tilde{A} = \cos\Theta$, isotropic radiation with $\tilde{A} = 1$ can be assumed. Instead of only emitting particles with $\tilde{B} = \frac{\pi}{2}$ into the source sphere, one can emit particles with $\tilde{B} = \pi$ in all directions.

$$N_I = A\ \mathrm{j}\ \Delta\mathrm{E}\ \Delta\mathrm{T} \int_0^{\tilde{B}} d\Theta\ \tilde{A} \sin\Theta \int_0^{2\pi} d\phi$$

Evaluating the integrals and equating with $j = N_C/(G\ \Delta E\ \Delta T)$ yields

$$j = \frac{N_I}{A\ \pi\ \Delta\mathrm{E}\ \Delta\mathrm{T}}; G = \frac{N_C}{N_I} A\pi\ \text{for} \tilde{A} = \cos\Theta; \tilde{B} = \frac{\pi}{2}$$

$$j = \frac{N_I}{A\ 2\pi\ \Delta\mathrm{E}\ \Delta\mathrm{T}}; G = \frac{N_C}{N_I} A\ 2\pi\ \text{for} \tilde{A} = 1; \tilde{B} = \frac{\pi}{2}$$

$$j = \frac{N_I}{A\ 4\pi\ \Delta\mathrm{E}\ \Delta\mathrm{T}}; G = \frac{N_C}{N_I} A\ 4\pi\ \text{for} \tilde{A} = 1; \tilde{B} = \pi$$

$$j = \frac{N_I}{A\ 4\pi\ \Delta\mathrm{E}\ \Delta\mathrm{T}}; G = \frac{N_C}{N_I} A\ 4\pi\ \text{for} \tilde{A} = \cos\Theta; \tilde{B} = \pi$$

Funding Part of the research described in this paper was carried out at the Jet Propulsion Laboratory, California Institute of Technology, under a contract with NASA (80NM0018D0004). ©2023. All rights reserved. Part of the research described in this paper was conducted at the Johns Hopkins University Applied Physics Laboratory under Europa Clipper Subcontract No. 1546282.

Declarations

Competing Interests The authors have no competing interests to declare that are relevant to the content of this article.

References

Adams L, Holmes-Siedle A (1978) The development of an MOS dosimetry unit for use in space. IEEE Trans Nucl Sci 25:1607–1612. https://doi.org/10.1109/TNS.1978.4329580

Addison P, Liuzzo L, Arnold H, Simon S (2021) Influence of Europa's time-varying electromagnetic environment on magnetospheric ion precipitation and surface weathering. J Geophys Res Space Phys 126:e2020JA029087. https://doi.org/10.1029/2020JA029087

Andriopoulou M, Roussos E, Krupp N, Paranicas C, Thomsen M, Krimigis S, Dougherty MK, Glassmeier K-H (2012) A noon-to-midnight electric field and nightside dynamics in Saturn's inner magnetosphere, using microsignature observations. Icarus 220:503–513. https://doi.org/10.1016/j.icarus.2012.05.010

Arnold H, Liuzzo L, Simon S (2020) Plasma interaction signatures of plumes at Europa. J Geophys Res Space Phys 125:e2019JA027346. https://doi.org/10.1029/2019JA027346

Bagenal F, Delamere PA (2011) Flow of mass and energy in the magnetospheres of Jupiter and Saturn. J Geophys Res Space Phys 116. https://doi.org/10.1029/2010JA016294

Bagenal F, Wilson RJ, Siler S, Paterson WR, Kurth WS (2016) Survey of Galileo plasma observations in Jupiter's plasma sheet. J Geophys Res, Planets 121:871–894. https://doi.org/10.1002/2016JE005009

Beck A (ed) (1972) Proceedings of the Jupiter radiation belt workshop. In: Beck AJ (ed) JPL technical memorandum. Jet Propulsion Laboratory, California Institute of Technology, Pasadena

Becker HN, Santos-Costa D, Jørgensen JL, Denver T, Adriani A, Mura A, Connerney JEP, Bolton SJ, Levin SM, Thorne RM, Alexander JW, Adumitroaie V, Manor-Chapman EA, Daubar IJ, Lee C, Benn M, Sushkova J, Cicchetti A, Noschese R (2017) Observations of MeV electrons in Jupiter's innermost radiation belts and polar regions by the Juno radiation monitoring investigation: Perijoves 1 and 3. Geophys Res Lett 44:4481–4488. https://doi.org/10.1002/2017GL073091

Berdis JR, Gudipati MS, Murphy JR, Chanover NJ (2020) Europa's surface water ice crystallinity: discrepancy between observations and thermophysical and particle flux modeling. Icarus 341:113660. https://doi.org/10.1016/j.icarus.2020.113660
Beutier T, Boscher D (1995) A three-dimensional analysis of the electron radiation belt by the Salammbô code. J Geophys Res Space Phys 100:14853–14861. https://doi.org/10.1029/94JA03066
Blöcker A, Saur J, Roth L (2016) Europa's plasma interaction with an inhomogeneous atmosphere: development of Alfvén winglets within the Alfvén wings. J Geophys Res Space Phys 121:9794–9828. https://doi.org/10.1002/2016JA022479
Bolton S, Janssen M, Thorne R, Levin S, Klein M, Gulkis S, Bastian T, Sault R, Elachi C, Hofstadter M, Bunker A, Dulk G, Gudim E, Hamilton G, Johnson W, Leblanc Y, Liepack O, McLeod R, Roller J, West R (2002) Ultra-relativistic electrons in Jupiter's radiation belts. Nature 415:987–991. https://doi.org/10.1038/415987a
Bolton SJ, Thorne RM, Bourdarie S, de Pater I, Mauk BH (2004) Jupiter's inner radiation belts. In: Bagenal F, Dowling T, McKinnon W (eds) Jupiter: the planet, satellites and magnetosphere. Cambridge University Press, Cambridge, pp 671–688
Breer BR, Liuzzo L, Arnold H, Andersson PN, Simon S (2019) Energetic ion dynamics in the perturbed electromagnetic fields near Europa. J Geophys Res Space Phys 124:7592–7613. https://doi.org/10.1029/2019JA027147
Brown ME, Hand KP (2013) Salts and radiation products on the surface of Europa. Astron J 145:110. https://doi.org/10.1088/0004-6256/145/4/110
Carbary JF (1980) Periodicities in the Jovian magnetosphere: magnetodisc models after Voyager. Geophys Res Lett 7:29–32. https://doi.org/10.1029/GL007i001p00029
Carlson RW, Hand KP (2015) Radiation noise effects at Jupiter's moon Europa: in-situ and laboratory measurements and radiation transport calculations. IEEE Trans Nucl Sci 62:2273–2282. https://doi.org/10.1109/TNS.2015.2460674
Carlson RW, Anderson MS, Johnson RE, Smythe WD, Hendrix AR, Barth CA, Soderblom LA, Hansen GB, McCord TB, Dalton JB, Clark RN, Shirley JH, Ocampo AC, Matson DL (1999a) Hydrogen peroxide on the surface of Europa. Science 283:2062–2064. https://doi.org/10.1126/science.283.5410.2062
Carlson RW, Johnson RE, Anderson MS (1999b) Sulfuric acid on Europa and the radiolytic sulfur cycle. Science 286:97–99. https://doi.org/10.1126/science.286.5437.97
Carlson RW, Anderson MS, Johnson RE, Schulman MB, Yavrouian AH (2002) Sulfuric acid production on Europa: the radiolysis of sulfur in water ice. Icarus 157:456–463. https://doi.org/10.1006/icar.2002.6858
Carlson RW, Anderson MS, Mehlman R, Johnson RE (2005) Distribution of hydrate on Europa: further evidence for sulfuric acid hydrate. Icarus 177:461–471. https://doi.org/10.1016/j.icarus.2005.03.026
Carlson R, Calvin WM, Dalton JB, Hudson GB, McCord RL, Moore MH (2009) Europa's surface composition. In: Pappalardo RT, McKinnon WB, Khurana KK (eds) Europa. University of Arizona Press, pp 283–327
Cassidy TA, Paranicas CP, Shirley JH, Dalton JB III, Teolis BD, Johnson RE, Kamp L, Hendrix AR (2013) Magnetospheric ion sputtering and water ice grain size at Europa. Planet Space Sci 77:64–73. https://doi.org/10.1016/j.pss.2012.07.008
Chyba CF (2000) Energy for microbial life on Europa. Nature 403:381–382. https://doi.org/10.1038/35000281
Clark RN, Fanale FP, Zent AP (1983) Frost grain size metamorphism: implications for remote sensing of planetary surfaces. Icarus 56:233–245. https://doi.org/10.1016/0019-1035(83)90036-2
Connerney JEP (1993) Magnetic fields of the outer planets. J Geophys Res 98:18659. https://doi.org/10.1029/93JE00980
Connerney JEP, Acuña MH, Ness NF (1981) Modeling the Jovian current sheet and inner magnetosphere. J Geophys Res Space Phys 86:8370–8384. https://doi.org/10.1029/JA086iA10p08370
Connerney JEP, Acuña MH, Ness NF, Satoh T (1998) New models of Jupiter's magnetic field constrained by the Io flux tube footprint. J Geophys Res Space Phys 103:11929–11939. https://doi.org/10.1029/97JA03726
Connerney JEP, Kotsiaros S, Oliversen RJ, Espley JR, Joergensen JL, Joergensen PS, Merayo JMG, Herceg M, Bloxham J, Moore KM, Bolton SJ, Levin SM (2018) A new model of Jupiter's magnetic field from juno's first nine orbits. Geophys Res Lett 45:2590–2596. https://doi.org/10.1002/2018GL077312
Connerney JEP, Timmins S, Herceg M, Joergensen JL (2020) A Jovian magnetodisc model for the Juno era. J Geophys Res Space Phys 125:e2020JA028138. https://doi.org/10.1029/2020JA028138
Council NR (2002) Signs of life: a report based on the April 2000 workshop on life detection techniques. The National Academies Press, Washington. https://doi.org/10.17226/10265
Davis MR, Meier RM, Cooper JF, Loeffler MJ (2021) The contribution of electrons to the sputter-produced O2 exosphere on Europa. Astrophys J Lett 908:L53. https://doi.org/10.3847/2041-8213/abe415

de Pater I, Dunn DE (2003) VLA observations of Jupiter's synchrotron radiation at 15 and 22 GHz. Icarus 163:449–455. https://doi.org/10.1016/S0019-1035(03)00068-X

de Soria-Santacruz M, Garrett HB, Evans RW, Jun I, Kim W, Paranicas C, Drozdov A (2016) An empirical model of the high-energy electron environment at Jupiter. J Geophys Res Space Phys 121:9732–9743. https://doi.org/10.1002/2016JA023059

Dessler AJ (1983) Physics of the Jovian magnetosphere. In: Axford WI, Hunt GE, Greely R (eds) Physics of the Jovian magnetosphere. Cambridge planetary science series. Cambridge University Press, New York

Divine N, Garrett HB (1983) Charged particle distributions in Jupiter's magnetosphere. J Geophys Res Space Phys 88:6889–6903. https://doi.org/10.1029/JA088iA09p06889

Drake F, Hvatum S (1959) Non-thermal microwave radiation from Jupiter. https://doi.org/10.1086/108047

Dulk GA, Leblanc Y, Sault RJ, Bolton SJ, Waite JH, Connerney JEP (1999) Jupiter's magnetic field as revealed by the synchrotron radiation belts. I. Comparison of a 3-D reconstruction with models of the field. Astron Astrophys 347:1029–1038

Fieseler P (2000) Master Thesis: the Galileo star scanner as an instrument for measuring energetic electrons in the Jovian Environment. Master Thesis, University of Southern California

Fieseler PD, Ardalan SM, Frederickson AR (2002) The radiation effects on Galileo spacecraft systems at Jupiter. IEEE Trans Nucl Sci 49:2739–2758. https://doi.org/10.1109/TNS.2002.805386

Fischer PD, Brown ME, Hand KP (2015) Spatially resolved spectroscopy of Europa: the distinct spectrum of large-scale chaos. Astron J 150:164. https://doi.org/10.1088/0004-6256/150/5/164

Fischer PD, Brown ME, Trumbo SK, Hand KP (2016) Spatially resolved spectroscopy of Europa's large-scale compositional units at 3–4 μm with Keck NIRSPEC. Astron J 153:13. https://doi.org/10.3847/1538-3881/153/1/13

Garrett HB, Jun I (2021) First adiabatic invariants and phase space densities for the Jovian electron and proton radiation belts—Galileo and GIRE3 estimates. J Geophys Res Space Phys 126:e2020JA028593. https://doi.org/10.1029/2020JA028593

Garrett HB, Levin SM, Bolton SJ, Evans RW, Bhattacharya B (2005) A revised model of Jupiter's inner electron belts: Updating the divine radiation model. Geophys Res Lett 32. https://doi.org/10.1029/2004GL021986

Garrett H, Jun I, Evans R, Kim W, Brinza D (2017) The latest Jovian-trapped proton and heavy Ion models. IEEE Trans Nucl Sci 64:2802–2813. https://doi.org/10.1109/TNS.2017.2755618

Gladstone GR, Persyn SC, Eterno JS, Walther BC, Slater DC, Davis MW, Versteeg MH, Persson KB, Young MK, Dirks GJ, Sawka AO, Tumlinson J, Sykes H, Beshears J, Rhoad CL, Cravens JP, Winters GS, Klar RA, Lockhart W, Piepgrass BM, Greathouse TK, Trantham BJ, Wilcox PM, Jackson MW, Siegmund OHW, Vallerga JV, Raffanti R, Martin A, Gérard J-C, Grodent DC, Bonfond B, Marquet B, Denis F (2017) The ultraviolet spectrograph on NASA's Juno mission. Space Sci Rev 213:447–473. https://doi.org/10.1007/s11214-014-0040-z

Goldsten JO, Maurer R, Peplowski PN, Holmes-Siedle AG, Herrmana CC, Mauk BH (2013) The engineering radiation monitor for the radiation belt storm probes mission. Space Sci Rev 179:485–502. https://doi.org/10.1007/s11214-012-9917-x

Grasset O, Dougherty MK, Coustenis A, Bunce EJ, Erd C, Titov D, Blanc M, Coates A, Drossart P, Fletcher LN, Hussmann H, Jaumann R, Krupp N, Lebreton J-P, Prieto-Ballesteros O, Tortora P, Tosi F, Van Hoolst T (2013) Jupiter ICy moons Explorer (JUICE): an ESA mission to orbit Ganymede and to characterise the Jupiter system. Planet Space Sci 78:1–21. https://doi.org/10.1016/j.pss.2012.12.002

Grundy WM, Buratti BJ, Cheng AF, Emery JP, Lunsford A, McKinnon WB, Moore JM, Newman SF, Olkin CB, Reuter DC, Schenk PM, Spencer JR, Stern SA, Throop HB, Weaver HA (2007) New horizons mapping of Europa and Ganymede. Science 318:234–237. https://doi.org/10.1126/science.1147623

Hand KP, Carlson RW (2011) H2O2 production by high-energy electrons on icy satellites as a function of surface temperature and electron flux. Icarus 215:226–233. https://doi.org/10.1016/j.icarus.2011.06.031

Hand KP, Carlson RW (2015) Europa's surface color suggests an ocean rich with sodium chloride. Geophys Res Lett 42:3174–3178. https://doi.org/10.1002/2015GL063559

Hand KP, Phillips CB, Murray A, Garvin JB, Maize EH, Gibbs RG (2009) Astrobiology and the potential for life on Europa. In: Pappalardo RT, McKinnon WB, Khurana KK (eds) Europa. University of Arizona Press, pp 589–629

Hand KP, Phillips CB, Murray A et al (2022) Science goals and mission architecture of the Europa lander mission concept. Planet Sci J 3:22. https://doi.org/10.3847/PSJ/ac4493

Hansen GB, McCord TB (2004) Amorphous and crystalline ice on the Galilean satellites: a balance between thermal and radiolytic processes. J Geophys Res, Planets 109. https://doi.org/10.1029/2003JE002149

Hao Y-X, Sun Y-X, Roussos E, Liu Y, Kollmann P, Yuan C-J, Krupp N, Paranicas C, Zhou X-Z, Murakami G, Kita H, Zong Q-G (2020) The formation of Saturn's and Jupiter's electron radiation belts by magnetospheric electric fields. Astrophys J Lett 905:L10. https://doi.org/10.3847/2041-8213/abca3f

Harris CDK, Jia X, Slavin JA, Toth G, Huang Z, Rubin M (2021) Multi-fluid MHD simulations of Europa's plasma interaction under different magnetospheric conditions. J Geophys Res Space Phys 126:e2020JA028888. https://doi.org/10.1029/2020JA028888

Holmes-Siedle A, Ravotti F, Glaser M (2007) The dosimetric performance of RADFETs in radiation test beams. In: 2007 IEEE radiation effects data workshop, pp 42–57. https://doi.org/10.1109/REDW.2007.4342539

Janesick J, Elliott T, Andrews J, Tower J, Bell P, Teruya A, Kimbrough J, Bishop J (2014) Mk x Nk gated CMOS imager. In: Proc. SPIE 9211, Target diagnostics physics and engineering for inertial confinement fusion III. International society for optics and photonics, p 921106. https://doi.org/10.1117/12.2063524

Jia X, Kivelson MG, Khurana KK, Walker RJ (2010) Magnetic fields of the satellites of Jupiter and Saturn. Space Sci Rev 152:271–305. https://doi.org/10.1007/s11214-009-9507-8

Jia X, Kivelson MG, Khurana KK, Kurth WS (2018) Evidence of a plume on Europa from Galileo magnetic and plasma wave signatures. Nat Astron 2:459–464. https://doi.org/10.1038/s41550-018-0450-z

Johnson RE, Carlson RW, Cooper JF, Paranicas C, Moore MH, Wong MC (2004) Radiation effects on the surfaces of the Galilean satellites. In: Bagenal F, Dowling T, McKinnon W (eds) Jupiter: the planet, satellites and magnetosphere. Cambridge University Press, Cambridge, pp 483–508

Jun I, Garrett HB (2005) Comparison of high-energy trapped particle environments at the Earth and Jupiter. Radiat Prot Dosim 116:50–54. https://doi.org/10.1093/rpd/nci074

Jun I, Ratliff JM, Garrett HB, McEntire RW (2002) Monte Carlo simulations of the Galileo energetic particle detector. Nucl Instrum Methods Phys Res A 490:465–475. https://doi.org/10.1016/S0168-9002(02)01072-0

Jun I, Garrett HB, Evans RW (2005a) High-energy trapped particle environments at Jupiter: an update. IEEE Trans Nucl Sci 52:2281–2286. https://doi.org/10.1109/TNS.2005.860747

Jun I, Garrett HB, Swimm R, Evans RW, Clough G (2005b) Statistics of the variations of the high-energy electron population between 7 and 28 Jovian radii as measured by the Galileo spacecraft. Icarus 178:386–394. https://doi.org/10.1016/j.icarus.2005.01.022

Jun I, Garrett HB, Cassidy TA, Kim W, Dougherty L (2019a) Updating the Jovian electron plasma environment. IEEE Trans Plasma Sci 47:3915–3922. https://doi.org/10.1109/TPS.2019.2901681

Jun I, Garrett HB, Evans RW (2019b) Trapped particle environments of the outer planets. IEEE Trans Plasma Sci 47:3923–3930. https://doi.org/10.1109/TPS.2019.2907069

Kammer JA, Hue V, Greathouse TK, Gladstone GR, Davis MW, Versteeg MH (2018) Planning operations in Jupiter's high-radiation environment: optimization strategies from Juno-UVS. In: Proc. SPIE 10699, Space telescopes and instrumentation 2018: ultraviolet to gamma ray. International society for optics and photonics, p 106993A. https://doi.org/10.1117/12.2312261

Khurana KK (1992) A generalized hinged-magnetodisc model of Jupiter's nightside current sheet. J Geophys Res Space Phys 97:6269–6276. https://doi.org/10.1029/92JA00169

Khurana KK (1997) Euler potential models of Jupiter's magnetospheric field. J Geophys Res Space Phys 102:11295–11306. https://doi.org/10.1029/97JA00563

Khurana KK, Schwarzl HK (2005) Global structure of Jupiter's magnetospheric current sheet. J Geophys Res Space Phys 110. https://doi.org/10.1029/2004JA010757

Khurana K, Vasyliūnas V, Mauk B, Frank L, Paterson B, Kivelson M, Krupp N, Woch J, Lagg A, Kurth B (2004) The configuration of Jupiter's magnetosphere. In: Bagenal F, Dowling T, McKinnon W (eds) In: Jupiter: the planet, satellites and magnetosphere, pp 593–616

Kim TK, Ebert RW, Valek PW, Allegrini F, McComas DJ, Bagenal F, Chae K, Livadiotis G, Loeffler CE, Pollock C, Ranquist DA, Thomsen MF, Wilson RJ, Clark G, Kollmann P, Mauk BH, Bolton S, Levin S, Nicolaou G (2020) Method to derive Ion properties from Juno JADE including abundance estimates for O+ and S2+. J Geophys Res Space Phys 125:e2018JA026169. https://doi.org/10.1029/2018JA026169

Kivelson MG, Bagenal F, Kurth WS, Neubauer FM, Paranicas C, Saur J (2004) Magnetospheric interactions with satellites. In: Bagenal F, Dowling T, McKinnon W (eds) Jupiter: the planet, satellites and magnetosphere. Cambridge University Press, Cambridge, pp 513–536

Kivelson MG, Khurana KK, Volwerk M (2009) Europa's interaction with the Jovian magnetosphere. In: Pappalardo RT, McKinnon WB, Khurana KK (eds) In: Europa. University of Arizona Press, pp 545–570

Klaasen KP, Breneman HH, Simon-Miller A, Banfield DJ, Levanas GC (2003) Operations and calibration of the solid-state imaging system during the Galileo extended mission at Jupiter. OE 42:494–509. https://doi.org/10.1117/1.1534590

Kollmann P, Roussos E, Paranicas C, Woodfield EE, Mauk BH, Clark G, Smith DC, Vandegriff J (2018) Electron acceleration to MeV energies at Jupiter and Saturn. J Geophys Res Space Phys 123:9110–9129. https://doi.org/10.1029/2018JA025665

Kollmann P, Paranicas C, Lagg A, Roussos E, Lee-Payne Z, Kusterer M, Smith D, Krupp N, Vandegriff J (2020) Galileo/EPD user guide. ESS Open Archive. https://doi.org/10.1002/essoar.10503620.1

Kollmann P, Clark G, Paranicas C, Mauk B, Roussos E, Nénon Q, Garrett HB, Sicard A, Haggerty D, Rymer A (2021) Jupiter's Ion radiation belts inward of Europa's orbit. J Geophys Res Space Phys 126:e2020JA028925. https://doi.org/10.1029/2020JA028925

Leblanc Y, Sault RJ, Dulk GA (1997) Synthesis of magnetospheric radio emissions during and after the Jupiter/SL-9 collision. Planet Space Sci 45:1213–1221. https://doi.org/10.1016/S0032-0633(97)00046-9

Ligier N, Poulet F, Carter J, Brunetto R, Gourgeot F (2016) VLT/SINFONI observations of Europa: new insights into the surface composition. Astron J 151:163. https://doi.org/10.3847/0004-6256/151/6/163

Lopes-Gautier R, McEwen AS, Smythe WB, Geissler PE, Kamp L, Davies AG, Spencer JR, Keszthelyi L, Carlson R, Leader FE, Mehlman R, Soderblom L, The Galileo NIMS and SSI Teams (1999) Active volcanism on Io: global distribution and variations in activity. Icarus 140:243–264. https://doi.org/10.1006/icar.1999.6129

Mauk BH (2012) Radiation belts of the solar system and universe. In: Summers D, Mann IR, Baker DN, Schulz M (eds) Dynamics of the Earth's radiation belts and inner magnetosphere. American Geophysical Union (AGU), pp 405–414. https://doi.org/10.1029/2012GM001305

Mauk BH, Mitchell DG, McEntire RW, Paranicas CP, Roelof EC, Williams DJ, Krimigis SM, Lagg A (2004) Energetic ion characteristics and neutral gas interactions in Jupiter's magnetosphere. J Geophys Res Space Phys 109. https://doi.org/10.1029/2003JA010270

Mauk BH, Haggerty DK, Jaskulek SE, Schlemm CE, Brown LE, Cooper SA, Gurnee RS, Hammock CM, Hayes JR, Ho GC, Hutcheson JC, Jacques AD, Kerem S, Kim CK, Mitchell DG, Nelson KS, Paranicas CP, Paschalidis N, Rossano E, Stokes MR (2017) The Jupiter Energetic Particle Detector Instrument (JEDI) investigation for the juno mission. Space Sci Rev 213:289–346. https://doi.org/10.1007/s11214-013-0025-3

Mauk BH, Haggerty DK, Paranicas C, Clark G, Kollmann P, Rymer AM, Peachey JM, Bolton SJ, Levin SM, Adriani A, Allegrini F, Bagenal F, Bonfond B, Connerney JEP, Ebert RW, Gladstone GR, Kurth WS, McComas DJ, Ranquist D, Valek P (2018) Diverse electron and Ion acceleration characteristics observed over Jupiter's main aurora. Geophys Res Lett 45:1277–1285. https://doi.org/10.1002/2017GL076901

Mauk BH, Clark G, Gladstone GR, Kotsiaros S, Adriani A, Allegrini F, Bagenal F, Bolton SJ, Bonfond B, Connerney JEP, Ebert RW, Haggerty DK, Kollmann P, Kurth WS, Levin SM, Paranicas CP, Rymer AM (2020) Energetic particles and acceleration regions over Jupiter's polar cap and main aurora: a broad overview. J Geophys Res Space Phys 125:e2019JA027699. https://doi.org/10.1029/2019JA027699

McCord TB, Hansen GB, Fanale FP, Carlson RW, Matson DL, Johnson TV, Smythe WD, Crowley JK, Martin PD, Ocampo A, Hibbitts CA, Granahan JC (1998) Salts on Europa's surface detected by Galileo's near infrared mapping spectrometer. Science 280:1242–1245. https://doi.org/10.1126/science.280.5367.1242

McCord TB, Hansen GB, Matson DL, Johnson TV, Crowley JK, Fanale FP, Carlson RW, Smythe WD, Martin PD, Hibbitts CA, Granahan JC, Ocampo A (1999) Hydrated salt minerals on Europa's Surface from the Galileo near-infrared mapping spectrometer (NIMS) investigation. J Geophy Res, Planets

Mitchell EH, Raut U, Teolis BD, Baragiola RA (2017) Porosity effects on crystallization kinetics of amorphous solid water: implications for cold icy objects in the outer solar system. Icarus 285:291–299. https://doi.org/10.1016/j.icarus.2016.11.004

Moore MH, Hudson RL (2000) IR detection of H2O2 at 80 K in Ion-irradiated laboratory ices relevant to Europa. Icarus 145:282–288. https://doi.org/10.1006/icar.1999.6325

Murakami G, Yoshioka K, Yamazaki A, Tsuchiya F, Kimura T, Tao C, Kita H, Kagitani M, Sakanoi T, Uemizu K, Kasaba Y, Yoshikawa I, Fujimoto M (2016) Response of Jupiter's inner magnetosphere to the solar wind derived from extreme ultraviolet monitoring of the Io plasma torus. Geophys Res Lett 43:12,308–12,316. https://doi.org/10.1002/2016GL071675

Nénon Q, Sicard A, Bourdarie S (2017) A new physical model of the electron radiation belts of Jupiter inside Europa's orbit. J Geophys Res Space Phys 122:5148–5167. https://doi.org/10.1002/2017JA023893

Nénon Q, Miller LP, Kollmann P, Liuzzo L, Pinto M, Witasse O (2022) Pitch angle distribution of MeV electrons in the magnetosphere of Jupiter. J Geophys Res Space Phys 127:e2022JA030627. https://doi.org/10.1029/2022JA030627

Neubauer FM (1980) Nonlinear standing Alfvén wave current system at Io: theory. J Geophys Res Space Phys 85:1171–1178. https://doi.org/10.1029/JA085iA03p01171

Neubauer FM (1998) The sub-Alfvénic interaction of the Galilean satellites with the Jovian magnetosphere. J Geophys Res, Planets 103:19843–19866. https://doi.org/10.1029/97JE03370

Neubauer FM (1999) Alfvén wings and electromagnetic induction in the interiors: Europa and Callisto. J Geophys Res Space Phys 104:28671–28684. https://doi.org/10.1029/1999JA900217

Nordheim TA, Hand KP, Paranicas CP (2018) Preservation of potential biosignatures in the shallow subsurface of Europa. Nat Astron 2:673–679. https://doi.org/10.1038/s41550-018-0499-8

Nordheim TA, Regoli LH, Harris CDK, Paranicas C, Hand KP, Jia X (2022) Magnetospheric ion bombardment of Europa's surface. Planet Sci J 3:5. https://doi.org/10.3847/PSJ/ac382a
Paranicas CP, Mauk BH, Krimigis SM (1991) Pressure anisotropy and radial stress balance in the Jovian neutral sheet. J Geophys Res Space Phys 96:21135–21140. https://doi.org/10.1029/91JA01647
Paranicas C, McEntire RW, Cheng AF, Lagg A, Williams DJ (2000) Energetic charged particles near Europa. J Geophys Res Space Phys 105:16005–16015. https://doi.org/10.1029/1999JA000350
Paranicas C, Carlson RW, Johnson RE (2001) Electron bombardment of Europa. Geophys Res Lett 28:673–676. https://doi.org/10.1029/2000GL012320
Paranicas C, Ratliff JM, Mauk BH, Cohen C, Johnson RE (2002) The ion environment near Europa and its role in surface energetics. Geophys Res Lett 29:18-1–18–4. https://doi.org/10.1029/2001GL014127
Paranicas C, Mauk BH, Khurana K, Jun I, Garrett H, Krupp N, Roussos E (2007) Europa's near-surface radiation environment. Geophys Res Lett 34. https://doi.org/10.1029/2007GL030834
Paranicas C, Cooper JF, Garrett HB, Johnson RE, Sturner SJ (2009) Europa's radiation environment and its effects on the surface. In: Pappalardo RT, McKinnon WB, Khurana KK (eds) Europa. University of Arizona Press, Tucson, pp 529–544
Paranicas C, Hibbitts CA, Kollmann P, Ligier N, Hendrix AR, Nordheim TA, Roussos E, Krupp N, Blaney D, Cassidy TA, Clark G (2018a) Magnetospheric considerations for solar system ice state. Icarus 302:560–564. https://doi.org/10.1016/j.icarus.2017.12.013
Paranicas C, Mauk BH, Haggerty DK, Clark G, Kollmann P, Rymer AM, Bonfond B, Dunn WR, Ebert RW, Gladstone GR, Roussos E, Krupp N, Bagenal F, Levin SM, Connerney JEP, Bolton SJ (2018b) Intervals of intense energetic electron beams over Jupiter's poles. J Geophys Res Space Phys 123:1989–1999. https://doi.org/10.1002/2017JA025106
Paranicas C, Szalay JR, Mauk BH, Clark G, Kollmann P, Haggerty DK, Westlake J, Allegrini F, Ebert RW, Connerney JEP, Bolton S (2021) Energy spectra near ganymede from Juno data. Geophys Res Lett 48:e2021GL093021. https://doi.org/10.1029/2021GL093021
Patterson W, Paranicas C, Prockter LM (2012) Characterizing electron bombardment of Europa's surface by location and depth. Icarus 220:286–290. https://doi.org/10.1016/j.icarus.2012.04.024
Plainaki C, Milillo A, Mura A, Orsini S, Cassidy T (2010) Neutral particle release from Europa's surface. Icarus 210:385–395. https://doi.org/10.1016/j.icarus.2010.06.041
Plainaki C, Cassidy TA, Shematovich VI, Milillo A, Wurz P, Vorburger A, Roth L, Galli A, Rubin M, Blöcker A, Brandt PC, Crary F, Dandouras I, Jia X, Grassi D, Hartogh P, Lucchetti A, McGrath M, Mangano V, Mura A, Orsini S, Paranicas C, Radioti A, Retherford KD, Saur J, Teolis B (2018) Towards a global unified model of Europa's tenuous atmosphere. Space Sci Rev 214:40. https://doi.org/10.1007/s11214-018-0469-6
Pospieszalska MK, Johnson RE (1989) Magnetospheric ion bombardment profiles of satellites: Europa and Dione. Icarus 78:1–13. https://doi.org/10.1016/0019-1035(89)90065-1
Poston MJ, Carlson RW, Hand KP (2017) Spectral behavior of irradiated sodium chloride crystals under Europa-like conditions. J Geophys Res, Planets 122:2644–2654. https://doi.org/10.1002/2017JE005429
Roussos E, Kollmann P, Krupp N, Paranicas C, Dialynas K, Sergis N, Mitchell DG, Hamilton DC, Krimigis SM (2018) Drift-resonant, relativistic electron acceleration at the outer planets: insights from the response of Saturn's radiation belts to magnetospheric storms. Icarus 305:160–173. https://doi.org/10.1016/j.icarus.2018.01.016
Rubin M, Jia X, Altwegg K, Combi MR, Daldorff LKS, Gombosi TI, Khurana K, Kivelson MG, Tenishev VM, Tóth G, van der Holst B, Wurz P (2015) Self-consistent multifluid MHD simulations of Europa's exospheric interaction with Jupiter's magnetosphere. J Geophys Res Space Phys 120:3503–3524. https://doi.org/10.1002/2015JA021149
Russell CT, Fieseler PD, Bindshadler D, Yu ZJ, Joy SP, Khurana KK, Kivelson MG (2001) Large scale changes in the highly energetic charged particles in the region of the Io torus. Adv Space Res 28:1495–1500. https://doi.org/10.1016/S0273-1177(01)00552-X
Saur J, Strobel DF, Neubauer FM (1998) Interaction of the Jovian magnetosphere with Europa: constraints on the neutral atmosphere. J Geophys Res, Planets 103:19947–19962. https://doi.org/10.1029/97JE03556
Schilling N, Neubauer FM, Saur J (2008) Influence of the internally induced magnetic field on the plasma interaction of Europa. J Geophys Res Space Phys 113. https://doi.org/10.1029/2007JA012842
Sicard A, Bourdarie S (2004) Physical electron belt model from Jupiter's surface to the orbit of Europa. J Geophys Res Space Phys 109. https://doi.org/10.1029/2003JA010203
Sicard-Piet A, Bourdarie S, Krupp N (2009) Jupiter radiation environment and effects tools-TN2: Part A-Trapped radiation belt model development (No. TN 2/13279 DESP). ONERA
Sicard-Piet A, Bourdarie S, Krupp N (2011) JOSE: a new Jovian specification environment model. IEEE Trans Nucl Sci 58:923–931. https://doi.org/10.1109/TNS.2010.2097276
Sittler EC, Strobel DF (1987) Io plasma torus electrons: Voyager 1. J Geophys Res Space Phys 92:5741–5762. https://doi.org/10.1029/JA092iA06p05741

Southwood DJ, Kivelson MG, Walker RJ, Slavin JA (1980) Io and its plasma environment. J Geophys Res Space Phys 85:5959–5968. https://doi.org/10.1029/JA085iA11p05959

Steffl A, Shinn A, Gladstone G, Parker J, Retherford K, Slater D, Versteeg M, Stern S (2013) MeV electrons detected by the Alice UV spectrograph during the New Horizons flyby of Jupiter. J Geophys Res Space Phys 117. https://doi.org/10.1029/2012JA017869

Stern SA, Slater DC, Scherrer J, Stone J, Dirks G, Versteeg M, Davis M, Gladstone GR, Parker JW, Young LA, Siegmund OHW (2008) ALICE: the ultraviolet imaging spectrograph aboard the new horizons Pluto–Kuiper belt mission. Space Sci Rev 140:155. https://doi.org/10.1007/s11214-008-9407-3

Tomás AT, Woch J, Krupp N, Lagg A, Glassmeier K-H, Kurth WS (2004) Energetic electrons in the inner part of the Jovian magnetosphere and their relation to auroral emissions. J Geophys Res Space Phys 109. https://doi.org/10.1029/2004JA010405

Trumbo SK, Brown ME, Hand KP (2019) H2O2 within chaos terrain on Europa's leading hemisphere. Astron J 158:127. https://doi.org/10.3847/1538-3881/ab380c

Truscott P, Heynderickx D, Sicard-Piet A, Bourdarie S (2011) Simulation of the radiation environment near Europa using the Geant4-based PLANETOCOSMICS-J model. IEEE Trans Nucl Sci 58:2776–2784. https://doi.org/10.1109/TNS.2011.2172818

Volwerk M, Khurana K, Kivelson M (2007) Europa's Alfvén wing: shrinkage and displacement influenced by an induced magnetic field. Ann Geophys 25:905–914. https://doi.org/10.5194/angeo-25-905-2007

Zhu BX, Lindstrom CD, Jun I, Garrett HB, Kollmann P, Paranicas C, Mauk BH, Gladstone GR (2021) Jupiter high-energy/high-latitude electron environment from Juno's JEDI and UVS science instrument background noise. Nucl Instrum Methods Phys Res A 1002:165244. https://doi.org/10.1016/j.nima.2021.165244

Authors and Affiliations

Richard Meitzler[1] · Insoo Jun[2] · Ryan Blase[3] · Timothy Cassidy[4] · Roger Clark[5] · Corey Cochrane[2] · Sam Fix[1] · Randy Gladstone[3] · John Goldsten[1] · Murthy Gudipati[2] · Kevin Hand[2] · Bryana Henderson[2] · Xianzhe Jia[6] · Joshua Kammer[3] · Peter Kollmann[1] · Alfred McEwen[7] · Heather Meyer[1] · Tom Nordheim[2] · Chris Paranicas[1] · Carol Paty[8] · Kurt Retherford[3] · Elias Roussos[9] · Abigail Rymer[1] · Todd Smith[1] · Joe Westlake[1] · Zach Yokley[1]

✉ I. Jun
Insoo.Jun@jpl.nasa.gov

1 Applied Physics Laboratory, John Hopkins University, Laurel, MD, USA

2 Jet Propulsion Laboratory, California Institute of Technology, Pasadena, CA, USA

3 Southwest Research Institute, San Antonio, TX, USA

4 Laboratory for Atmospheric and Space Physics, University of Colorado Boulder, Boulder, CO, USA

5 Planetary Science Institute, Tucson, AZ, USA

6 University of Michigan, Ann Arbor, MI, USA

7 University of Arizona, Tucson, AZ, USA

8 University of Oregon, Portland, OR, USA

9 Max Planck Institute for Solar System Research, Goettingen, Germany